

PROPERTIES OF EXPLOSIVELY DRIVEN ALUMINUM PARTICLE
FIELDS AND THEIR INHALATION HAZARDS

By

CHARLES MICHAEL JENKINS

A DISSERTATION PRESENTED TO THE GRADUATE SCHOOL
OF THE UNIVERSITY OF FLORIDA IN PARTIAL FULFILLMENT
OF THE REQUIREMENTS FOR THE DEGREE OF
DOCTOR OF PHILOSOPHY

UNIVERSITY OF FLORIDA

2012

© 2012 Charles Michael Jenkins

To my wife Jean, and children Jenna, Keith, Chris, Eric and Patrick and also my father Charlie; and for my mother June who I wish more than anything had been able to see this day come true, thanks for everything.

ACKNOWLEDGMENTS

For me this has been a long path to get to this point for a number of reasons. I have had great support from family, friends, and faculty (many of whom I now consider friends) at the university. For my immediate family I am sure that it has seemed like a never ending effort. To my wife, Jean, who put up with the many late nights, my year away at the University, and my paperwork messes on the kitchen table, thanks for your support. To my children Jenna, Keith, Chris, Eric, and Patrick I give my thanks for the support you provided while making the time used seem painless to you, even though this effort did take away from your needs as well. I would also like to thank Dr. Bob Sierakowski and Dr. Ron Armstrong for the encouragement to continue my quest and to the others at the Wright Laboratory who provided me support during my year at the University, making my work at the Munitions Directorate the least of my concerns. My special thanks to my senior advisor and mentor Dr. Chang-Yu Wu in the Environmental Engineering and Sciences Department for providing me the opportunity to reach my goal by sponsoring me, allowing me to prove that an old dog can learn new tricks and for the new and interesting knowledge he provided me in his classes and mentoring sessions. To the other members of my graduate committee Dr. Stephen Roberts, Dr. Wesley Bolch, Dr. Meng-Dawn Cheng, Dr. Kevin Powers, and Dr. Ben Koopman who provided not only the opportunity to learn something new and help me reach my goal but who also provided the extra effort to aid me in starting back into an academic environment that has changed considerably since I was last a full time student. Also to Dr. Stephen Roberts, Dr. Wesley Bolch, Dr. Mark Brown and Dr. Brij Moudgil, thanks for the delightful courses whose content were very different from anything I had ever had and held my interest at all times. A special thanks also to Dr. Kevin Powers, who first

posed the question to me during my first visit to the University “Why not get your PhD?” which made me think that it might be possible and who helped me answer many questions during this effort both academically and otherwise. To Dr. Meng-Dawn Cheng who went out of his way on many occasions for special help secessions concerning hands on of aerosol equipment not available at the university. Also my thanks to Dr. Hassan El-Shall at the Particle Engineering and Research Center (PERC) who was my first contact at the PERC for directing me to the right people and being helpful with my initial questions concerning particle technology and the PERC’s capabilities. Additionally, thanks to Dr. Yasuyuki Horie who provided me with access to his wealth of knowledge and insight into the many details of shock physics and numerical simulation as well as providing me with the opportunity to be introduced to his friends and colleagues in the field of multiphase flow and shock physics.

I would also like to thank Dr. Walt Kozumbo and Dr. Bill Wilson for providing much of the funding for my research, making it possible to complete my research by providing the resources and opportunity to study in Gainesville. Also to the other personnel at the High Explosive Research & Development facility at Eglin AFB for approval and public release under 96ABW-2009-0235, 96ABW-2011-0255, 96ABW-2012-0094 for Chapters 2 through 4 and release number 96ABW-2012-0122 for the entire dissertation. Finally, to my parents, thanks for the support, encouragement and interest in this endeavor.

TABLE OF CONTENTS

	<u>page</u>
ACKNOWLEDGMENTS.....	4
LIST OF TABLES.....	8
LIST OF FIGURES.....	9
ABSTRACT	11
CHAPTER	
1 INTRODUCTION TO ALUMINUM ENERGETICS	13
Early History	13
Characterization of Explosively Driven Metallic Particle Fields.....	15
Material Health Hazards	17
Objectives	20
2 PARTICLE VELOCITY AND STRUCTURES IN BLAST WAVES IMAGED USING PARTICLE IMAGE VELOCIMETRY.....	22
Introduction	22
Experimental Setup	23
Results.....	26
Conclusions	29
3 EXPLOSIVELY DRIVEN PARTICLE FIELDS IMAGED USING A HIGH SPEED FRAMING CAMERA AND PARTICLE IMAGE VELOCIMETRY.....	37
Introduction	37
Experimental Setup and Methodology	40
Numerical Simulation	44
Particle Concentration Estimates	47
Shock Induced Momentum Transfer	48
Results.....	49
Analysis	50
Image Processing.....	50
Particle Velocity and Concentration.....	52
Early Time Powder Front Velocities	54
Particle, Fireball and Shock Interaction	56
Particle Velocity Gradient within the Particle Field	60
Experimental Reproducibility	61
Conclusions	62

4	IN VITRO DISSOLUTION AND SIMULATION STUDIES OF ALUMINUM POWDER USED IN HIGH EXPLOSIVE AND REACTIVE MIXTURES	83
	Introduction	83
	Materials and Methods.....	86
	Solvent Preparation.....	87
	Dissolution.....	87
	Results and Discussion.....	94
	Conclusion	97
5	SUMMARY	106
	APPENDIX: CENTER OF MASS PROGRAM FOR PARTICLE FIELDS	111
	LIST OF REFERENCES	113
	BIOGRAPHICAL SKETCH.....	118

LIST OF TABLES

<u>Table</u>	<u>page</u>
3-1 Charge mass properties	78
3-2 Mesh resolution for PIV dispersion simulation	79
3-3 Experimental HSFC, PIV and numeric velocity values	80
3-4 Mesh resolution sensitivity study	81
3-5 Experimental and simulation derived drag coefficients with shock velocity interaction time ratio	82
4-1 Composition of Simulated Lung Ultra-Filtrate (SUF).....	98
4-2 Aluminum volume weighed mean particle size parameters and dissolution rate constants	99

LIST OF FIGURES

<u>Figure</u>	<u>page</u>
2-1 Test charge quality check.....	31
2-2 PIV test setup (top down), high explosive was set above the light sheet with particle flow in a downward direction.....	32
2-3 PIV images of H-10	33
2-4 Velocity contour plot for the particle region outlined for H-10 was cropped for ease of processing.....	34
2-5 Raw image of camera's FOV enhanced using pseudo color without background subtraction for Valimet H-95 aluminum powder.....	35
2-6 H-95 powder velocity contour plot	36
3-1 PIV test setup (view top down), high explosive was set above the light sheet with particle flow in a downward direction.....	64
3-2 Early time expansion of powders and fragments imaged with HSFC	65
3-3 Early time experimental and numerical expansion data plotted.....	66
3-4 H-10 particle fields moving from top to bottom, at 44.7 cm from charge.....	67
3-5 Particle and shock front trajectory for H10.....	68
3-6 Particle and shock front trajectory for H-95	69
3-7 Particle and shock front trajectory for W-27.....	70
3-8 Fragment and shock velocity for a 22.1 g solid case.....	71
3-9 Representation of a PIV image with velocity gradient for H-95 powder series. ..	72
3-10 Mean particle velocity vs. shot number series within the FOV.....	73
3-11 Composite of H-10 simulation, visual and laser images.....	74
3-12 Composite of H-95 simulation, visual and laser images.....	75
3-13 Composite of W-27 simulation, visual and laser images.....	76
3-14 Composite of solid case particle simulation, visual and laser images.....	77

4-1	Scanning electron micrograph (SEM) of H-2 aluminum powder used in the dissolution tests.....	100
4-2	Image of one dissolution setups	101
4-3	Sketch of dissolution cell with stir bar in the center under filter holder.....	102
4-4	Dissolution plot for H-2 aluminum in SUF.....	103
4-5	PSD for H-2 D[4,3] and the adjusted section for D[4,3] ₁ with an arithmetic std of $\sigma \leq 0.5$	104
4-6	A plot of the remaining mass fractions of inhaled aluminum.....	105

Abstract of Dissertation Presented to the Graduate School
of the University of Florida in Partial Fulfillment of the
Requirements for the Degree of Doctor of Philosophy

PROPERTIES OF EXPLOSIVELY DRIVEN ALUMINUM PARTICLE FIELDS AND
THEIR INHALATION HAZARDS

By

Charles Michael Jenkins

August 2012

Chair: Chang-Yu Wu

Major: Environmental Engineering Sciences

A high speed framing camera (HSFC) and a particle image velocimetry (PIV) instrument were used to determine the properties of explosively driven particle fields in microsecond and millisecond intervals. Two-inch long right circular cylindrical charges with half-inch diameter cores made of organic explosive were used as the driving explosive. The core was surrounded by a particle bed of aluminum or tungsten powder of a specific particle size distribution. Position data from the leading edge of the particle fronts for each charge were recorded with the framing camera at early time, first 125 μ s, and with a PIV instrument at later time (5.7 ms) to determine the mean particle velocities. In addition, using a PIV image, a velocity gradient along the length of the particle field was established by using the mean particle velocity value determined from three separate horizontal bands that transverse the particle field. The results showed lower velocity particles at the beginning of the particle field closest to the source and higher velocity particles at the leading front portion of the field. Differences in particle dispersal, luminescence, and agglomeration were seen when changes in the initial particle size and material type were made. The aluminum powders showed extensive luminescence with agglomeration, forming large particle structures while a tungsten

powder showed little luminescence, agglomeration and no particle structures.

Combining velocity data from the HSFC and PIV, the average drag coefficient for each powder type was determined. The particle field velocities and drag coefficients at one meter showed good agreement with the numerical data produced from a computational fluid dynamics code.

The dissolution rate of aluminum powder in serum ultrafiltrate stimulant solution was conducted. A match to the International Commission on Radiological Protection, ICRP 66 lung model default value for the overall instantaneous clearance rate was determined. Using a ratio of volume moments derived from the sample powder system, a correction to the experimental dissolution rate constant was made to fit a mono distributed powder system that will allow the constant to be applied to other powder systems with different particle size distributions.

CHAPTER 1 INTRODUCTION TO ALUMINUM ENERGETICS

Early History

Circumstantial evidence exists that the invention of gunpowder occurred early in the 3rd – 4th century BC by the alchemist Ge Hong (Liang 2006); however, it was not until the Wujing Zongyao, "Collection of the Most Important Military Techniques", written between 1031 – 1044 AD that the specific formulation was revealed. Later, during Renaissance in Europe (1400-1500) the Italians began to create exploding shells and military rockets with mixtures of metal powders and charcoal capable of exploding at the maximum altitude. Eventually by 1830 the Italians using the advances in chemistry identified potassium chlorate as a new oxidizer that burned faster and hotter than potassium nitrate which allowed the use of new colors and brighter fireworks (Bradley 2002). Eventually, as aluminum became available and inexpensive (1 dollar per Kg) after Charles Martin Hall's breakthrough discovery in 1886 of passing electrical current through a molten mixture of Cryolite (Na_3AlF_6) and aluminum oxide (Al_2O_3), it then found its application in high explosives. When aluminum was added to nitrated explosives like nitrocellulose or trinitrotoluene (TNT), it was discovered that it provided significant energy to the formulation and greatly enhanced the explosive's blast effect. The blast effect can be described as an increase in the duration and amplitude of the reinforcing pressure wave produced from the expanding light product gases and heated air following behind the initial shock front from the detonation of the explosive. The enhancement of rapid oxidation from materials in or surrounding the high explosive can result, if strong and rapid enough, in the creation of a re-enforcing shock wave with a longer duration pressure impulse or blast wave following behind the Taylor wave. The

Taylor wave is the rarefaction wave which brings the product gas of the explosive from the state of the detonation products behind the detonation front to their fully expanded state at ambient pressure.

Although energetic materials have been used for many years and have been studied in detail for their performance and properties, many of the details of heat and energy transfer particularly along the shock front and within the fireball are still unknown due to incomplete models with simplified chemistry and mixed equations of state (Schmitt et al. 2010) and the lack of experimental data to validate the different proposed numerical models (Frost and Zhang 2006). Numerical calculations can provide a deeper understanding and predictive capability for various phenomena of both ideal and non-ideal explosives, particularly at extreme conditions that are not readily accessible by current experimental measurements (Schmitt et al. 2010). Due to the relatively little fundamental research performed to characterize conditions such as flow expansion and energy partitioning, predictive numerical models are largely absent (Schmitt et al. 2010).

The selection of the proper particle size distribution and mass quantity of metallic powder as the fuel is critical to ensure that the released energy reacts in time to support the blast wave; otherwise, ignition may not occur in the proper time domain to support the primary shock. Intrusion of hot product gases along with shock compression of the material at early time (10-15 μ s) provides the energy necessary to fracture, melt and ignite the metal fuel with the proper oxidizing environment. Confinement of the explosive by a case increases the exposure duration experienced by the particles to the hot product gases and enhances the particle shock compression and burning. In this regard, Tanguay et al. (2006) stated that “control of the adiabatic expansion rate of the

detonation products plays a significant role” for the critical diameter for particle ignition. Zhang et al. (2003) and Ripley et al. (2007) described the shock interaction time with the particles as the primary mechanism for heating based on changes in internal energy at the interaction time scales. Detonation, the propagation of reaction wave controlled by shock waves, typically occurs in time scales of microseconds to nanoseconds at the meso-scale (i.e. individual particle motion) and even shorter time periods at the molecular level (i.e. bond breaking). Currently the primary theory guiding shock wave and explosive detonations is provided by the ZND model developed separately but concurrently in the 1940s by Zel’dovich (1940); von Neumann (1963); Döring (1943). The model admits to a finite-rate chemical reaction which is initiated at a high pressure point known as the von Neumann spike which is a compression of the explosive with an infinitely thin shock wave. The relaxation to the Chapman-Jouguet Chapman, D. (1899) condition produces the detonation product gas that expands backward and forms the blast wave that can entrain particles.

Characterization of Explosively Driven Metallic Particle Fields

Many researchers in the field of energetics and multi-phase flow are in great need of experimental data to aid in the validation of numeric models. This situation was identified by Frost and Zhang (2006) when they stated that, “currently challenges remain related to the development of robust in situ diagnostics for probing the flow parameters such as particle and gas temperature, pressure and particle density and velocity within the multiphase fireball.” Without validation, the numeric models can only hint at the possible material and dynamic outcomes of multi-phase flow simulation.

How energy in the expansion process is partitioned between particulate and gas products remains a subject of intense research, but it is known to differ depending on

the explosive formulation and the particle characteristics (Zarei et al. 2011). The degree of energy transferred to the particulate solids depends on several factors including, the material morphology, mass fraction, material type, particle and packing density, confinement geometry including particle bed thickness (Zarei et al. 2011; Tanguay et al. 2007). All of these factors have an effect on the initial particle bed expansion rate, shock transmission at early time and the later expansion process. These factors can have a significant effect on particle agglomeration, structure formation, particle burn rate and dynamics of the particle flow field. Particle-particle interaction (i.e. collisions), particle fluid (i.e. wake effects), and shock compression of the particle bed and surrounding air are also believed to be significant aspects which contribute to the dynamic process (Zarei et al. 2011). This is especially the case in early time “upon the passage of the detonation wave through the metal particles which accelerates the particles in a non-uniform manner” during initial expansion when particle concentration is high (Zarei et al. 2011).

Because these phenomena are being modeled and incorporated into simulation programs, experimentally determined velocity values are needed at the individual particle and particle field level to support improved numeric results and validation of the postulated models. The use of PIV in a hot sooty environment was demonstrated in the high-speed exhaust plume of a solid rocket motor using naturally occurring particles as the tracers (Balakumar and Adrian, 2004). For short duration events, PIV has also been demonstrated for dispersed olive oil droplets using an exploding bridge wire (Murphy et al. 2005). Techniques which gather quality data are therefore paramount for

understanding phenomena at the meso-scale and required for validation in the modeling community of the complex flows resulting from explosively driven particle fields.

Material Health Hazards

The primary health hazard from the material being used in this research is the handling of the high explosives 1,3,5-trinitro-1,3,5-triazine (RDX) and octahydro-1,3,5,7-tetranitro-1,3,5,7-tetrazocane (HMX); each explosive charge was capable of producing severe injury or death. The explosive was impact and electrostatic sensitive, which requires special safety handling procedures at even steps in the build-up of the charges and their testing. Additionally, the mixing, loading and detonation of an energetic material generates large numbers of particulate products containing nano, submicron and a range of micron size particulates (Cheng & Jenkins, 2005) which can also present a hazard to anyone not protected and unaware of the hazards.

The recognition of ill health associated with high levels of ultra-fine particles in urban pollution episodes with increases in cardiovascular deaths was identified by Seaton et al. (1995). Currently the interest is in particulate sizes in the range <100 nm; these are considered harmful and may lead to thickening in blood plasma (Peters et al 1997; Donaldson et al. 2005) and are in the same size range as many manmade engineered nanomaterials (Buxton et al. 2003; Ferrari 2005; Donaldson et al. 2008). When inhaled, some materials and sizes have the capacity for translocation from the lung to other parts of the body such as the bone marrow, spleen, lymph nodes and heart (Oberdörster et al. 2005). Movement of nanoparticles along axons and dendrites of neurons has been observed as well as toxicity in the form of oxidative stress through the formation of reactive oxygen species (ROS) adjacent to particles in cellular and subcellular structures (Oberdörster et al. 2005).

Specifically addressing aluminum and alumina nanoparticles, Braydich-Stolle et al. (2005) identified significant toxic effects to C18-4 Germine stem cells from 30 and 50 nm aluminum particles. They were found to promote plasma membrane leakage and mild mitochondrial dysfunction at concentrations of 50 µg/mL. Wagner et al. (2007) using 30 and 40 nm Al₂O₃ particles and 50, 80, and 120 nm Al particles with 2-3 nm oxide coats determined the differences of rat alveolar macrophages in their cytotoxicity and the reduction in phagocytotic ability. They determined that “aluminum nanoparticles showed chemical-composition-dependent toxicity where Al-NP was consistently more toxic than the Al₂O₃-NP and had less phagocytotic ability”. Cytotoxicity may not be the only adverse effect of nanoparticles; they may also affect the immunological response of cells where the surface coating defines much of their bioactivity (Lewinski et al. 2008). Additionally, Oesterling et al. (2008) demonstrated that “alumina nanoparticles increase mRNA and protein expression which leads to increased adhesiveness shown by induction of vascular cellular adhesion molecule-1 (VCAM-1), intercellular adhesion molecule-1 (ICAM-1), and P- and E-selectins (ELAM-1) as well as monocyte adhesion to vascular endothelial cells and that exposure of these materials “may increase risk for development of inflammatory diseases such as atherosclerosis”.

Until recently, exposure to nanomaterials was neither identified nor deemed to be of any particular consequence. Exposure from the toxic effects of known virgin energetic and post detonation materials were thought to be mild and completely mitigated by the use of personal protective equipment (PPE) developed for gas products and submicron and micron particulates. The use of a combination of a face mask with HEPA and carbon filters, over coat, and procedures to limit or reduce

exposure using ventilation (dilution) was the norm. With the determination that large numbers of nano particulates are produced from combustion and the detonation of explosives (Cheng and Jenkins 2005) along with the increased use of engineered nanomaterials in explosive formulation ingredients, exposure to these materials became a growing concern. Handling procedures for nano sources and their concentration levels within laboratories, as well as processes and procedures to reduce the likelihood of exposure given are being reevaluated, that even HEPA filters are not 100% effective. Research into methods for predicting and monitoring levels of exposure to nanomaterials is becoming a significant effort on the part of laboratories engaged in nano materials research. The realization of the possible dangers to workers health identified by recent research has provided the driving force to find ways to mitigate and to quantify the level of exposure.

The research provided in this paper supports a method to estimate and monitor exposure of different tissue compartments to nanoaluminum with greater confidence in the default value for clearance to blood provided in the ICRP Publication 66. By correcting the rate constant after completion of the dissolution process with volume moments, the use of polydistributed rather than monodistributed powder samples can simplify the processing of samples, reducing the need for some specialized equipment and allows for the creation of a single exponential equation needed in the new full recycling simulation models like the nano version of the Integrate Modules for Bioassay Analysis (nano IMBA) currently under a joint development effort with the University of Florida, the Biokinetic Modeling and Dosimetry Group of Oak Ridge National Laboratory and the UK Health Protection Agency and IMBA staff.

Objectives

The specific objectives investigated in this research pertain to the phenomena of particle dynamics in blast waves and the determination of the dissolution rate constant of aluminum powder with an oxide coat. Objective 1 was to demonstrate the capability of using PIV in imaging high speed particles under the adverse conditions and short event times present with multi-phase flow in the post detonation environment. The first objective was made possible using a high speed framing camera (HSFC) and adapting an off-the-shelf particle image velocimetry instrument for use with explosives. Objective 2 was to use the combined established capability of a high speed framing camera and PIV to estimate particle drag coefficients. Objective 3 was to examine and identify unusual two phase phenomena from different charge configurations and particle sizes and compare the results to a solid metal case baseline. Objective 4 was to compare experimentally derived velocity and drag coefficients to the numerical model values derived from a computational fluid dynamics (CFD) code at the same time step. Simulation conditions were adjusted for the charge weights and powder materials with the numerical results compared to the experimental data. This process produced graphical plots and statistical mean values from the numerical values.

Objective 5 was tied to the toxicological portion of the thesis to determine the clearance rate constant (λ) and the accuracy of the default dissolution rate constant by experimental means and compare its value to the ICRP 66 lung model default value. The clearance rate constant (λ) in the form of a single decaying exponential was derived and compared to the ICRP value. Objective 6 was to adjust the dissolution rate constant for H-2 spherical aluminum using volume moments derived from the initial PSD into a dissolution rate that would represent the dissolution rate for a mono-distributed

PSD. An equation in Mercer format for eventual use in the ICRP-66 lung model was established for use in the Integrated Modules of Bioassay Analysis (IMBA) numeric model. This toxicological work will provide greater assurance that the ICRP dissolution rate constant is accurate and demonstrate a method to correct the rate constants of poly-distributed powders using a method of volume moments.

CHAPTER 2 PARTICLE VELOCITY AND STRUCTURES IN BLAST WAVES IMAGED USING PARTICLE IMAGE VELOCIMETRY

Introduction

Energetic formulations frequently contain various quantities of reactive metallic particles to increase energy content for blast wave enhancement. The initial mass fraction of the metal powder as well as the particle size and morphology all influence the extent to which the particle combustion couples with blast wave propagation (Frost and Zhang, 2006). The initial shock and particle combustion process provides energy resulting in some amount of energy transfer into particle inertia. Inertia transferred to particulates with different sizes and densities within the blast wave has significant effects on particle dynamics and structure formation within the blast wave. As a result, both the particle flow field and blast wave generated by the detonation of a heterogeneous explosive in a free field differ from that of an ideal homogeneous explosive (Frost and Zhang, 2006). Currently, challenges remain related to the development of robust in-situ diagnostics for probing the flow parameters such as particle and gas temperature, pressure, and particle density and velocity within the multiphase fireball (Frost and Zhang, 2006). While multiphase flow in blast waves has been a subject of interest for many researchers, the specifics of heat and energy transfer are not fully understood due in part from the lack of experimental methods capable of measuring particle motion and gas flow without exterior interference. Particle image velocimetry (PIV) is a means of obtaining high resolution images of particle flow. Balakumar and Adrian (2004) demonstrated the ability to image and perform vector analysis on high velocity non-uniform particles imbedded in solid rocket motor materials and for short duration events it has been demonstrated that PIV can be used to image

olive oil droplets dispersed by exploding bridge wires (Murphy et al. 2005). However, no study using a PIV system for determining particle velocity and structure has been reported for explosively driven metallic particles.

The research reported in this communication describes the application of PIV to obtain velocity and particle interaction phenomena. Examples of processes occurring within the blast wave that were observed in the images included particle structure formation, particle velocity information, and particle agglomeration.

Experimental Setup

A PIV system was used in this research with some portions of the optics modified to provide protection from the harsh environment produced during the detonation of a high explosive (H.E.). The system used a 120 mJ pulsed laser (Model YAG120-15, Big Sky Laser, Quantel) that was frequency doubled from 1064 nm to 532 nm. The Nd:YAG twin cavity pulsed system had a pulse width of 12 ns and was capable of a repetition rate of 15 Hz. Additional system equipment included a synchronizer for control of image and laser timing made by TSI Inc. (Model 610035) capable of 1 ns resolution and TSI Inc. software (Insight 3G) installed on a Dell Precision desk top system for laser, camera control and image processing. Band pass filters of 532 + 2/-0 nm from Andover Inc. (PN 532FS10-50) were used to reduce the filtered light due to luminosity through the camera lens and enhance the particle's image while providing protection of the CCD imaging chip. The imaging system used a Power View Plus 11MP camera from TSI Inc (Model No.630062) with a square pixel size of 9 μm and a Nyquist resolution limit of 55 pixels/mm. The camera was fitted with a 105 mm Nikkor lens (Model No. 610044) made by Nikon and set at an f-number = 11. The standoff distance

from the light sheet to the surface of the outer lens was 83.8 cm (33 in.) making the magnification about 0.1 M.

The test item used a core of organic explosive made from four stacked $\frac{1}{2} \times \frac{1}{2}$ in. cylindrical pellets glued together totaling 10.3 g. Their composition includes 98.5% 1,3,5-trinitro-1,3,5-triazine (RDX) and 1.5% Viton, a fluoro elastomer used as a binder to ensure dimensional stability. Polydispersed aluminum powders used in the tests included H-10 and H-95 made by Valimet Inc. from their spherical powder series, these materials had mean volumetric diameters of 15 μm (H-10) and 129 μm (H-95) and were generally log normally distributed. The powders were used to fill the annular space between the wall of the paper tube and the RDX core (Figure 2-1) and provided the tracer particles for PIV tracking.

To ensure repeatable results, the charge configuration was maintained and only the metallic powder nominal diameter was changed for each test series. The internal diameter of the paper tube was built to 1.00 ± 0.006 in. by Yazoo Mills Inc. The annular space of 6.35 mm thickness was maintained by using end caps to center the explosive core. All charges were built by the same technician using the same method of construction. X-ray images of the test items (Figure 2-1) were conducted on all charges to ensure no defects such as air gaps or miss alignment of the glued pellets were incorporated into the test charges. A serial number was provided for each charge and a record of dimensional and mass attributes was retained.

To ensure good image quality of the aluminum powders within the FOV, the camera lens was pre-focused on dispersed olive oil droplets within the light sheet prior to start of the experiments. This was accomplished with an atomizer, using a Devilbiss

heavy duty air compressor (Model No. 8650D) and a DeVilbiss atomizer (Model No. 163) with a Laskin nozzle to produce 1–2 μm diameter particles as individual light-scattering markers (Murphy et al. 2005). The small low velocity oil droplets have good light reflectance and thus provided a sharp bright image for focusing. Test charges used in the experiment were hung above the light sheet from a test fixture in a position where the axial centerline of each charge was aligned with the projected laser light sheet (Figure 2-2). This ensured that particle flow was parallel to the light sheet and perpendicular to the camera. The arrangement provided a particle flow in a downward direction towards the test chamber's floor (Figure 2-2). The vertical placement of the charge was in a position 83.82 cm from the upper right corner of the camera's field of view (FOV). The lower edge of the FOV was about 1 meter from the chamber's floor. A grid panel of dimension 4 ft wide and 8 ft tall with one centimeter blocks was placed behind the charge prior to firing the charge, it stretched from the charge's hanging position through the FOV and down to the chamber's floor. The grid panel was used to map the charge position with relation to the camera's FOV (18.5 x 28.5 cm), allowing the position of any particle image or structure to be correlated to the position of the charge for later analysis. Each test charge position was recorded with a handheld camera and a video image of the FOV position was made with the PIV camera; this set of images also included a spatial calibration standard. The test standard was recorded before the start of each series with the test charge number recorded in both the PIV software and the setup image.

The light sheet distance from the camera's lens was set at 83.82 cm and checked after each test for movement. To ensure particles fell within the PIV camera's FOV, a

timing delay for the first image was established at 5.8 ms using the detonator fire pulse from the facility's fire control system. The fire pulse was split and sent to the PIV system software and to the charge's detonator. A difference in cable lengths accounted for only about a 10 ns difference in pulse arrival times (1 ns/m) between software and detonator. The delay time interval between the fire pulse and image A was chosen based on the estimated particle velocity from previous high speed video tests. The Dt value between image A and image B for H-10 powder was 80 μ s with a delay time of 5.8 ms and a Dt value for H-95 of 50 μ s with a delay time of 5.6 ms. These Dt times were later refined for image displacements of 10–15 pixels in subsequent tests after image analysis had been performed on the first image pairs. The reduction in the time between image frames enhanced the spatial resolution by reducing the size of interrogation regions used in the vector analysis.

Results

An example of a raw image can be seen in Figure 2-3a. Image preprocessing via background subtraction was used to enhance the particle's image by decreasing the luminescence produced by the H.E. and burning aluminum (Figure 2-3b) seen in the images as a light white haze. The analysis process entailed a numerical estimate of background luminosity for each image; this value was subtracted from the entire image. Each image must be processed separately with its own background estimate because of the variances from image to image. The light sheet thickness was set at about 1.0 mm in the camera's FOV; this was checked via burn paper during the initial setup for each series of powder sizes. Controlling light sheet thickness can be challenging considering the several protective glass structures, mirror and the gas cloud the beam must pass through before it reaches the camera's FOV.

The proper selection and combination of processing algorithms can significantly influence the analysis product by increasing the number of valid vectors in the flow. The most effective grid engine processor provided in the TSI analysis software for this series of experiments proved to be a Recursive Nyquist Grid Engine and the Hart Correlation approach for the Correlation Engine. The Gaussian Mask was used for the Spot Mask Engine and Gaussian Peak Engine for the Peak Engine while using rectangular interrogation regions. Post-processing used a local validation processor and vector field conditioning setup. A universal median test was used for local validation to remove bad vectors; the universal median is an improved median filter which is a more robust validation method than the mean because the tolerance is less sensitive to the flow field. For vector field conditioning the local median was used for filling holes in the interrogation regions which failed validation. The resulting vector analysis yielded approximately 4500 total vectors in each image, of which about an average of 71.5% were good and the balance interpolated. Most of the bad vectors were associated with the initial analysis from images within the dense structures or those on the inside edge of a structure where the second image comingled within a dense structure. Velocity vector errors and lost images are believed to have primarily fell into three categories (1) images lost from in and out of plane motion (2) images which were lost from high background luminosity or (3) those lost within structures where the structures were so dense that individual particle images could not be determined.

The presences of wave-like structures seen in Figure 2-3 were regions determined to be of high particle concentration and velocity while regions of low particle concentration are often associated with lower particle velocities with few velocity vectors

supporting the flow. The distribution of these regions can best be seen in the velocity contour plot shown in Figure 2-4, where velocities are in meters per second. Velocity contour patterns do not always match exactly with their raw images because of the limitations of PIV at high particle concentration to resolve individual particle images from overlapping images and from losses due to invalid images. Invalid images can be common in this type of flow and lost image pairs can mean a greater number of interpolated vectors are needed to fill holes in otherwise dense particle flow regions. The combination of low velocity, particle voids, a lack of valid image vectors, rotating flow areas, and the shape of the region of interest (ROI, shown boxed in red) selected for analysis can significantly affect the image's statistical values. A very broad range of velocity values were seen over the ROI in most of the processed images for these tests.

Zhang et al. (2001) discusses the ability of very fine particles to equilibrate to the flow of the combustion products whereas larger particles will respond slowly due to their large inertia. Adrian (1991) described the particle lag $|v-u|$ resulting from the single particle slip velocity equation due primarily from the mismatch between fluid and particle density with the larger particle diameters of the same material showing greater velocity separation than the smaller particles. Due to the wide standard deviation (SD) of both of the particle systems, H-10 had a SD = 9.5 μm and the H-95 SD = 34.64 μm , it is likely that this had some influence in the distribution of the particle flow patterns.

$$|\mathbf{v} - \mathbf{u}| = \left| \frac{2\rho_p d_p}{3\rho C_D} |\dot{\mathbf{v}}| \right|^{1/2} \quad (2-1)$$

where v is the Lagrangian particle velocity, u is the Eulerian fluid velocity, C_D is the drag coefficient, ρ_p and ρ are the particle and fluid densities and d_p is the particle diameter.

For the larger particle size tested, under the same conditions, significantly less wave-like structures were seen. Greater steepness and luminosity with increased directionality in the particle flow in the y-direction was also observed as can be seen in Figure 2-5 where background subtraction has not been applied. These observations may be explained in part from the delayed response to acceleration from the shock wave and expanding product gas of the larger H-95 particles.

For H-10, Figure 2-4, shows smaller more numerous vector groupings and about 12.0 m/s slower mean velocity than for the H-95 plot in Figure 2-6. With the explosive charges kept in the same initial position in Figure 2-3 as in Figure 2-5, a shift in the ROI position along the x-axis, shown boxed, can be seen in the two images. This result indicates a smaller x-directional component to the left for particles in the contour plots of Figure 2-6 than for the particles in Figure 2-4 for the H-10 powder.

Conclusions

In summary it has been shown that capturing images of particles driven by a high explosive is possible and can provide high quality images resulting in good velocity data. Results from the two different aluminum powder sizes showed that within the blast wave there is a significant difference in particle velocities, structure, resultant particle direction and luminosity. Low vector yield or large numbers of bad vectors can be expected if numerous particle structures exist, particularly, if individual images are not well defined as in a dense structure; in such cases good validation settings are required to remove bad vectors. This may not be a concern for the experimenter if the primary goal of the research is to identify particle phenomena rather than determining fluid velocities in the surrounding gas. Higher velocities in the FOV for H-95 than for H-10 may be related to the inertia properties of the larger particles resisting deceleration as

compared to the H-10 of lower mass. The variation in inertia values of the different diameter particles would also explain the greater x-axis velocity component or translation along the x-axis for H-10. Hot spots, regions of very high velocity in the contour plot are likely the result of miss identified images resulting from high density particle concentrations or irregular shaped particle images, while three sigma variations in velocity are expected to be shown based on existing software settings. Additional research is continuing with different particle size distributions, charge configurations and material type.

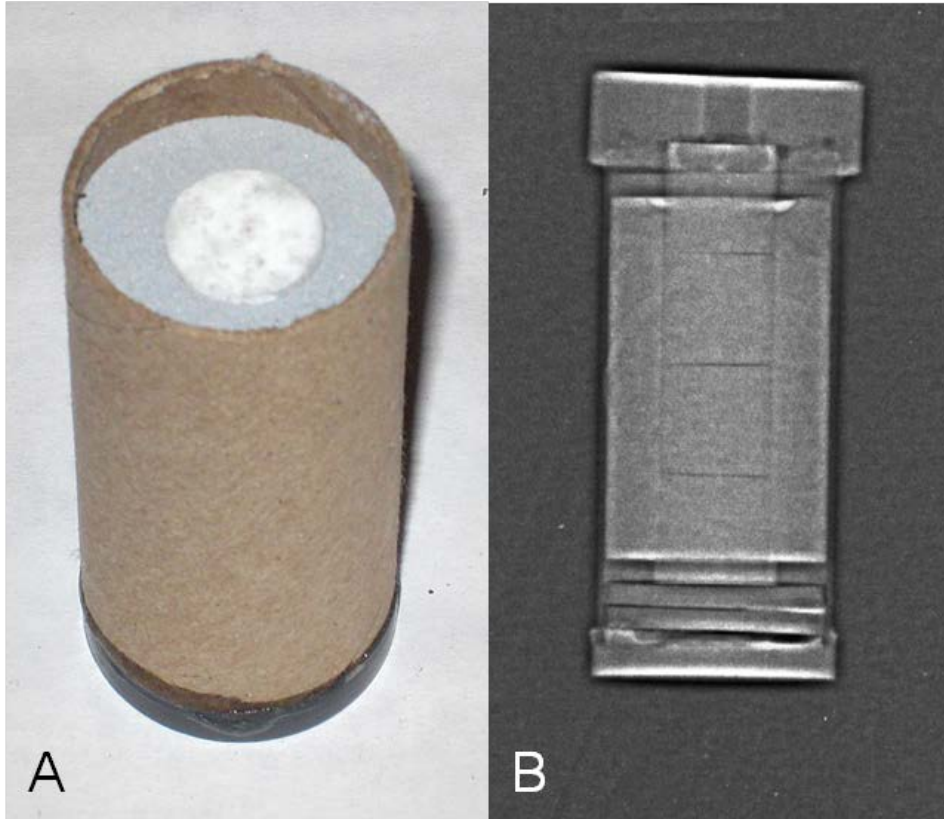


Figure 2-1. Test charge quality check. A) Annular test charge configuration for powder systems B) X-ray of charge to ensure against defects.

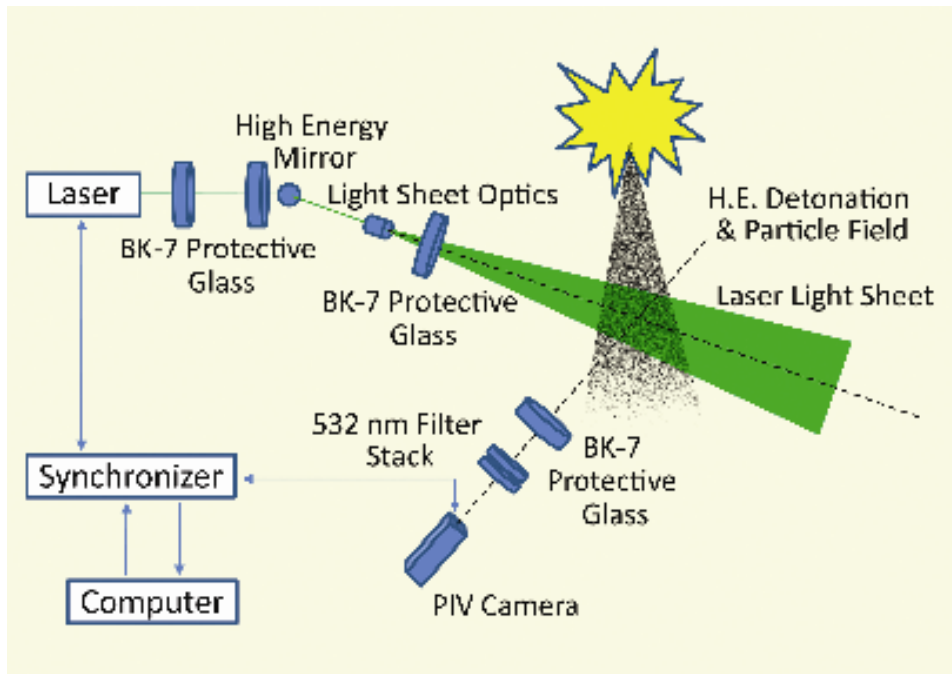


Figure 2-2. PIV test setup (top down), high explosive was set above the light sheet with particle flow in a downward direction.

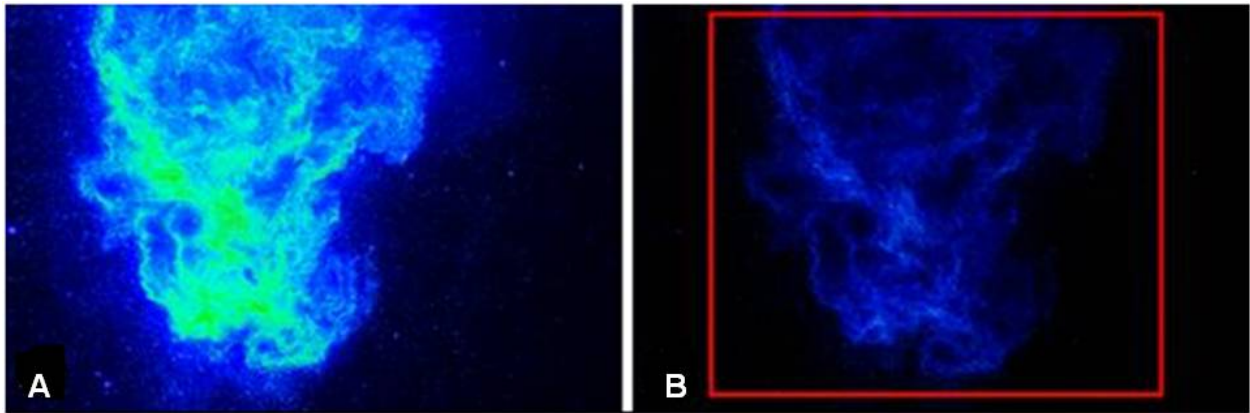


Figure 2-3. PIV images of H-10. A) Raw image of camera's FOV with enhanced using pseudo color to highlight particle structures, B) background subtraction used to reduce luminosity and highlight individual particles for improved vector analysis.

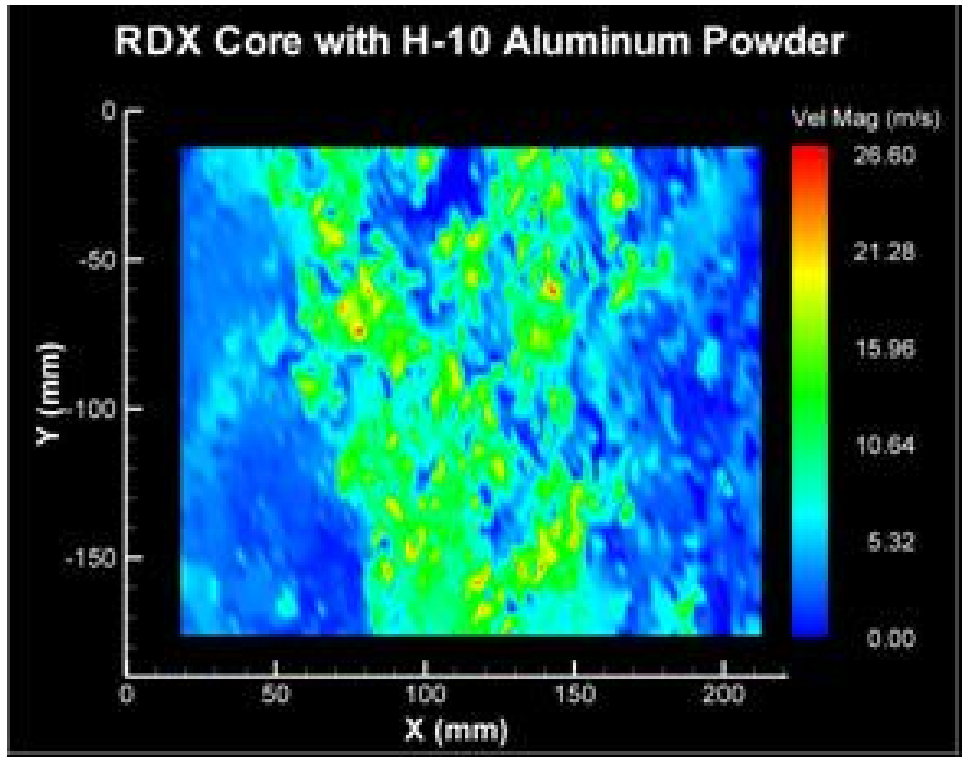


Figure 2-4. Velocity contour plot for the particle region outlined for H-10 was cropped for ease of processing. X & Y dimensions correspond to dimensions of the FOV.

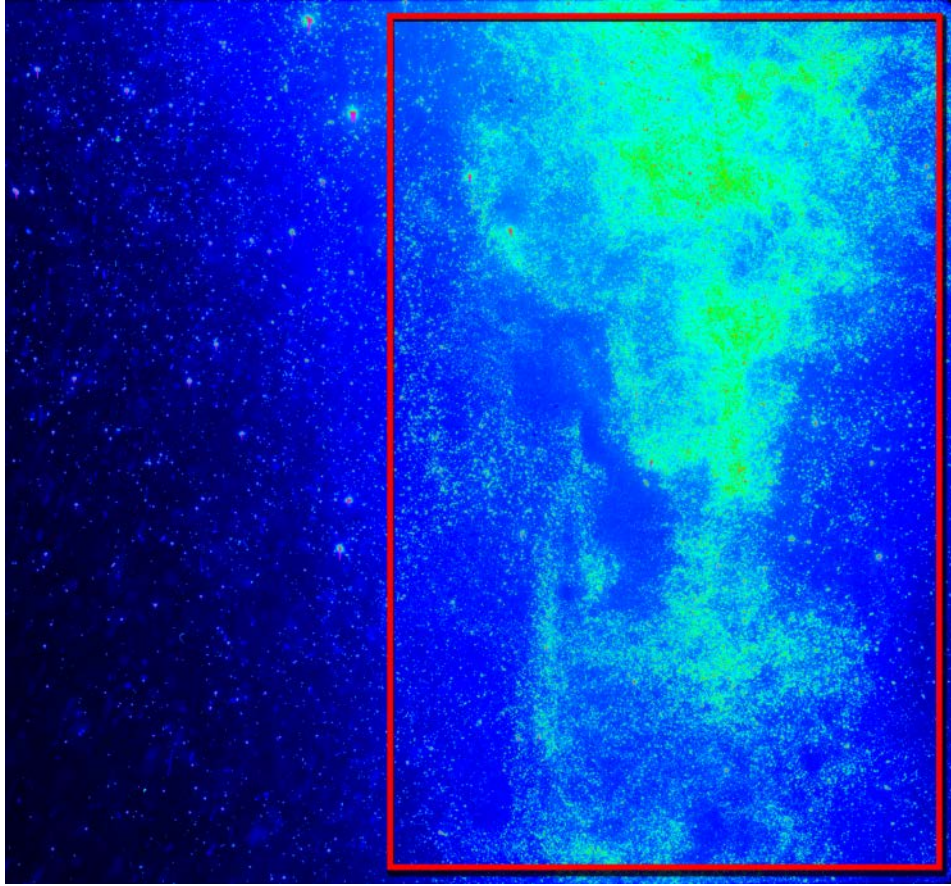


Figure 2-5. Raw image of camera's FOV enhanced using pseudo color without background subtraction for Valimet H-95 aluminum powder.

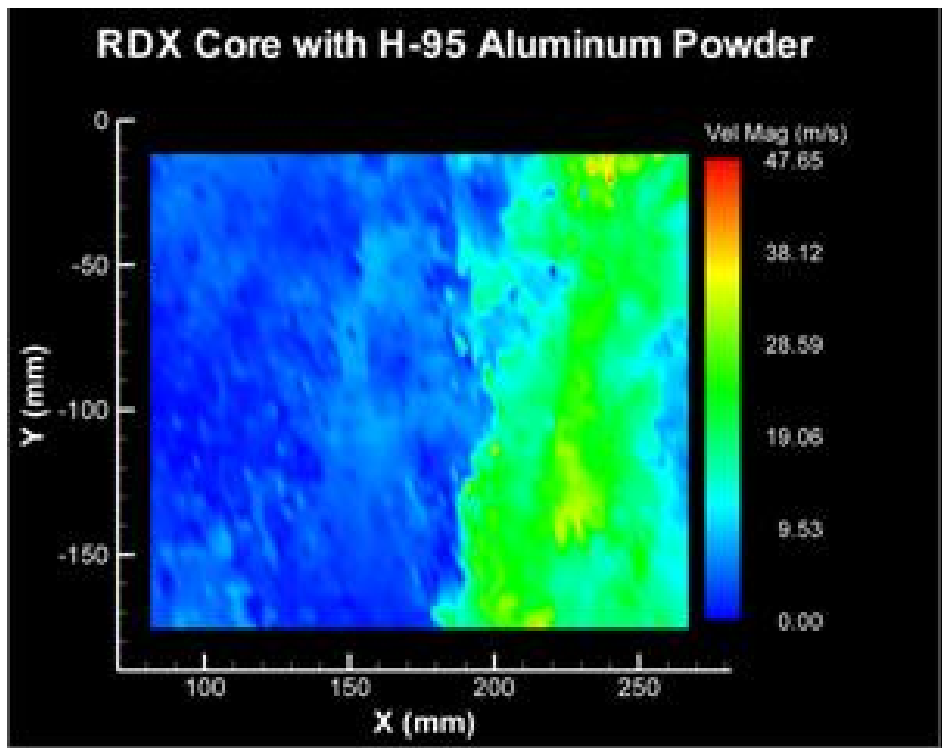


Figure 2-6. H-95 powder velocity contour plot for the particle region outlined in Figure 2-5.

CHAPTER 3 EXPLOSIVELY DRIVEN PARTICLE FIELDS IMAGED USING A HIGH SPEED FRAMING CAMERA AND PARTICLE IMAGE VELOCIMETRY

Introduction

Detonation of a heterogeneous explosive provides momentum and energy transfer from the explosive to the solid particles within or packed around the outer shell of an explosive medium. The particles become accelerated from the rapidly expanding product gases, generating a two-phase flow of material into the surrounding environment. If the explosive contains metallic particles which are reactive under high temperature and pressure and they have the correct morphology, ignition of the particles may take place if oxidizing gases are present (Frost et al. 2007). However, if inert particles are used in the explosive or ignitions of the reactive particles are delayed sufficiently until the particle number falls to a low count, the energy release will not add to the blast wave (Frost et al. 2007). Experimental studies have been conducted by Zhang et al. (2001) and Frost et al. (2007) using inert steel particles and by Frost et al. (2005, 2007) with reactive aluminum and magnesium particles. Each of these experiments used sensitized nitro methane as the driving explosive and each were compared with numerical predictions.

In addition to particle collisions, particles are thought to have significant influence on shock transmission and are affected by turbulent flows resulting in localized regions of anomalously high or low particle concentrations (Eaton and Fessler 1994). The availability and comparison of experimental data with the output of numerical simulations yields an opportunity to improve numerical models and provide a greater understanding of particle and shock interaction in mixed media flows. Numerical shock wave investigations of this type have been reviewed by Saito et al. (2003), Zhang et al.

(2003), Engelhardt (2008), Donahue et al. (2007), Ling et al. (2009) and Dunbar et al. (2011) for modeling specific to this research. An additional review of momentum transfer due to the interaction of shock waves with solid particles was provided by Zhang et al. (2003) where the relationships of particle shock interaction time and velocity relaxation time was described. This phenomenon occurs when the particle crosses the shock front and the ratio of the particle interaction time to the particle velocity relaxation time provides a criterion for determining whether a change in the particle velocity is significant due to the shock interaction. Accurate measurement of particle velocity is therefore critical to assess momentum and energy transfer from the gas medium to the solid particle phase. Despite the use of high speed cameras and other image based methods, Frost and Zhang (2006) stated that currently challenges remain related to the development of robust in situ diagnostics for probing the flow parameters such as particle and gas temperature, pressure, particle density, and velocity within the multiphase fireball because of the complexities of the particle field.

Ling et al. (2009) using a shock-tube problem studied the gas-particle flow arising from particle-laden driver sections. Time scales for equilibrium of the expansion fan, particles contact, and the shock wave were estimated; determining that particle laden flows behind the shock affected the speed and intensity of the shock front.

Balakrishnan et al. (2010) has conducted three-dimensional simulations of inert multiphase particle systems in which he varied the particle size and volume fraction to calculate the gas and particle momentum flux and impulse loading. The method applies an approach using the Discrete Equation Method (DEM) with the use of an Eulerian-

Lagrangian two phase model for dense phase particle flow, shock and gas phase interaction.

In studies cited earlier, methods used to collect velocity and impulse data included flash x-ray and high speed video for imaging particle fields and momentum traps, blast pressure “lollipop” gauges and particle streak gauges using various means of mechanical measurement with numerical calculation. The non-imaging techniques for the most part average small areas of the blast wave which may contain a heterogeneous distribution of particles and may not be representative of the entire flow field. Additionally, these techniques have traditionally not provided information specific to individual or small groups of 10-15 particles. Particle image velocimetry (PIV) has the ability to provide information specific to individual particles, as in particle tracking velocimetry (PTV) a subset of PIV when the flow field has low image densities. In regions of higher image density PIV can provide a resultant velocity vector for groups of well defined particle images as described by Adrian (1991). PIV is capable of providing information on particle position, size, velocity and concentration under certain conditions. Published work has demonstrated the feasibility of performing PIV measurements in the hot, high-speed exhaust plume of a solid rocket motor using naturally occurring particles (Balakumar and Adrian, 2004). For short duration events, PIV has also been demonstrated with olive oil droplets dispersed by an exploding bridge wire can be imaged and velocities determined (Murphy et al. 2005). The use of PIV for imaging explosively driven metallic particles was provided by Jenkins et al. (2010).

Small scale testing of explosively loaded items have become experimentally attractive because of the high cost associated with testing large items and the ability to

provide larger numbers of test items for greater confidence in statistical evaluations. Gagliardi et al. (2005) noted that small-scale tests are initially used to obtain a useful amount of data from a small amount of explosives, considering safety, cost, and speed of production and that small-scale testing is very useful. Information on scalability of small charges, particle turbulence and dispersal are also of benefit for enhancement of numeric models.

This paper is organized as follows, in Section 2 the Methodology of test set-up is described, numerical model and its assumptions, the characteristics by which the data and images will be evaluated. In Section 3 the results from the tests are presented and in Section 4 the analyses of the data is conducted. In the final Section the conclusions of the analyses is presented. The objectives of this paper are to describe the use of a high speed framing camera (HSFC) and a PIV instrument for determining particle field velocities and drag coefficients for aluminum and tungsten powders of different sizes and comparing numerical values generated using a computational fluid dynamics code (CFD) modeled for the experimental setup conditions.

Experimental Setup and Methodology

The basic setup (Figure 3-1) was the same as that reported by Jenkins et al. (2010) using the same PIV instrumentation and test support equipment with a few exceptions identified in this study. The optics box, laser and camera portal windows for this study were made from 0.5 inch sapphire material with an anti-reflective coating provided by Crystal Systems Inc. These windows were produced by the heat exchanger method (HEM) and had a 60/40 polished surface quality on the faces and a surface peak to valley (PV) flatness better than 2λ at 633 nm. The material and coating was specified to reduce the energy reflectance at 532 nm from 5% per interface

determined with BK-7 glass, used in previous reported tests (Jenkins et al. 2010), to less than 0.25% per interface. Optical flatness and parallelism was improved to less than 5 arc minutes due to the increased flatness of the sapphire.

Hot aluminum and tungsten particles are broad band emitters that emit 532 nm light. A filter stack was used to remove all frequencies except 532 ± 2 nm light and to reduce luminosity across the remaining spectrum from burning and hot particles; this helped prevent over saturation of the imaging chip. The reduction in light transmission was between 50% and 55% through each filter in the stack. The filter stack was varied between 2-3 filters depending on the expected brightness of the test event. The camera was fitted with a 105 mm Nikkor lens (Model No. 610044) made by Nikon and set at an f-number = 4.5. The f-number was reduced from previous work in order to decrease the depth of field and reduce the number of ghost images produced from the hot particles which have 532 nm light as a component in their spectrum. These images were outside of the light sheet but within the depth of field of the lens. The standoff distance from the light sheet to the surface of the outer lens was 81.3 cm (32 inches) making the magnification 0.1 M. The position locations of the equipment in the test chamber were checked for movement after each shot to ensure continued alignment for the follow-on shots.

The test items contained a core of organic explosive made from four stacked $\frac{1}{2}$ x $\frac{1}{2}$ inch cylindrical pressed pellets, pressed to 90% theoretic maximum density (crystal density) and glued together into a single 5.08 cm stick. The mass of explosive used in this research totaled 11.18 g of material, equating to 95.3% of octahydro-1,3,5,7-tetranitro-1,3,5,7-tetrazocane (HMX) high explosive (HE) with 4.7% weight of a binder to

ensure dimensional stability. The detonator used to initiate the explosive was an RP-2 exploding bridge wire (EBW) containing 18 mg of pentaerythritol tetranitrate (PETN) giving a percentage of just 0.16% of the total explosive. The RP-2 has a function time of 1.65 μs with a standard deviation (STD) of less than 0.035 μs .

Metallic powders were used to fill the annular space between the wall of a paper tube and the HMX explosive core; the particles acted as the natural tracer particles for PIV tracking. The aluminum powders H-10 ($d_p = 13.4 \mu\text{m}$) and H-95 ($d_p = 113.4 \mu\text{m}$) were used in addition with charges containing the tungsten powder W-27 ($d_p = 34.5 \mu\text{m}$) as a comparison to the known lower density and reactive aluminum powders. The particle size distributions (PSD) were determined using a laser diffraction particle analyzer (LS13320, produced by Beckman-Coulter). All powder charges were filled to their tap density; the physical attributes of the charges are listed in Table 3-1. To provide a baseline for comparison with the powder charges, a solid aluminum shell case made of 6061-T6 wall thickness of 3.2 mm was tested.

Initial particle expansion was imaged using a high speed framing camera (HSFC) (model # 114, produced by Cordon). Test charges were positioned along the top edge of a grid board with 2.54 cm blocks and detonated using a split fire pulse to initiate the camera. Examples of the images produced are provided in Figure 3-2 where the imaging duration was 5 μs per-frame for 25 frames on color slide film. These images provided particle front formation, velocity information and identification of early time combustion for the first 125 μs . Early time particle front and solid case fragment velocities are shown in Figure 3-3.

The distance from the surface position to the leading edge of the particle front was done at discrete time intervals from a position within the middle 25% of the charge. Adjustments within this position were done to account for instabilities in the particle front resulting from jetting or particle flow not perpendicular to the charge surface. Measurement positions once set within the 25% region were not adjusted to ensure that the proper flow progression was repeatedly measured. Measurement error included the maximum variation in the leading edge of the particle front, and any variation in the boundary between the particle front and air resulting from inadequate lighting or camera focusing.

To ensure reproducible test results, control of the charge configuration and powder volume was maintained within each series. Additionally, multiple test firings of each configuration were performed for statistical validity. The charge volume was controlled by having the internal diameter of the paper tube built to 1.00 ± 0.006 inch which maintained an annular space of 6.35 mm between the explosive core and the tube wall. X-ray images were made of all the test charges to ensure no defects such as air pockets in the powder or misalignment of the glued explosive pellets were incorporated into the test charges. Spatial calibration for the PIV instrument was accomplished by using a traceable ruler (MR-1) made by Geller Microanalytical Laboratory. The ruler for a 10 mm increment has an uncertainty of ± 0.0025 mm and is traceable to the National Physical Laboratory in the United Kingdom.

For the PIV imaging, each test charge was hung 218.4 cm from the chamber floor. The position was recorded with a digital photograph from a small hand held camera and a video image of the field of view (FOV) location was made using the PIV camera

against a 1 cm marked grid backdrop. The light sheet thickness for all PIV shots were checked prior to each test via burn paper and were measured to be 1.0 mm at the center of the camera FOV. A set of setup images were recorded each time before the start of every test with the test charge number recorded in both the setup image and PIV software test item file. Image delay time between the fire pulse and first PIV image for the powder series was set at 5.7 ms. Delay times for the solid case was 0.95 ms and for the special early time image of H-10 (Figure 3-4), a delay time of 2.5 ms was used.

A 7.5 volt transistor-transistor logic (TTL) signal from the fire control hardware was split and sent to both the PIV system software and the charge detonator. A difference in cable lengths accounted for only about a 15 ns difference in pulse arrival times (5 ns/m) between computer software and the detonator in the explosive train.

Numerical Simulation

Numerical simulations were conducted on the metal powders and solid shell test item configurations. A simplified model was chosen of the Basset-Boussinesq-Oseen (BBO) equation. From Poelma (2004) some simplifications to the BBO equation can be made if the particle Reynolds number is small and the ratio of the particle density to the fluid density ($\rho_p/\rho_t \gg 1$), then the Stokes drag term and the gravity effects become dominant. The magnitude of the gravitational velocity contribution to the mean velocity of the particle fields were considered during the 5.7 μ s time of flight (TOF) chosen for this study. Because the gravitation effect becomes negligible at this time duration to less than 1 mm/s, all body forces were neglected. The simplified model described by Tanguay et al. (2007) where body forces such as gravity on a particle in the detonation

products is only subject to a drag force was therefore assumed. Thus by Newton's second law:

$$m \frac{dv_p}{dt} = \frac{1}{2} C_D A_{cs} \rho_t |u_t - v_p| (u_t - v_p) \quad (3-1)$$

where m is the mass of the particle, A_{cs} is the projected area of the particle, C_D is the total drag coefficient, ρ_t is the density of the fluid and u_t and v_p are the fluid and particle velocities. The charges used in this study had a particle bed of 6.35 mm thick in the annular space surrounding the charge. Mechanical interactions between the condensed explosive and the particle bed used the equation of state (EOS) identified in Zhang et al. (2003) for the Euler solutions; there was no EOS used during the Lagrangian portion of the expansion.

The volumetric content of the solids was high in the dispersed mixture phase; therefore the Smirnov (1988) equation for higher values of the friction coefficient was used during the initial distribution phase and is represented as:

$$C_D = \begin{cases} C_1 = \left(\frac{24}{Re_p} + \frac{4.4}{Re_p^{0.5}} + 0.42 \right) & \frac{\alpha_3}{\alpha_1 + \alpha_3} \leq 0.08 \\ C_2 = \frac{4(\alpha_1 + \alpha_3)}{3\alpha_1} \left(1.75 + \frac{150\alpha_3}{\alpha_1 Re_p} \right) \kappa_1, & \frac{\alpha_3}{\alpha_1 + \alpha_3} \geq 0.45 \\ \frac{(0.92\alpha_3 - 0.08\alpha_1)C_2 + (0.45\alpha_1 - 0.55\alpha_3)C_1}{0.37(\alpha_1 + \alpha_3)}, & 0.08 < \frac{\alpha_3}{\alpha_1 + \alpha_3} < 0.45 \end{cases} \quad (3-2)$$

$$\kappa_1 = \left(\frac{\rho_w}{\rho_1} \right)^{4/5} \left(\frac{\mu_w}{\mu_1} \right)^{1/5} \quad (3-3)$$

$$Re_p = \frac{\rho_1 |u_1 - u_3| d_p}{\mu_w} \quad (3-4)$$

where C_D is the drag coefficient and κ_1 is the compressibility factor of the gas, Re_p is the particle Reynolds number, α_1 and α_3 are the volumetric concentrations in the gas

and solid phase, μ_1 and μ_w is the dynamic viscosity in the gas phase and film around the particle. The density of the fluid in the gas phase is ρ_1 and the density at the particle surface by the film is represented as ρ_w .

The Klyachko drag equation (Fuchs 1964) was used to estimate the drag coefficient for the H-10, H-95 and W-27 particles during the intermediate and later time when the particle concentration was less than 0.08 in the second and third mesh adjustment. Additionally, drag coefficient (C_D) values were calculated in the simulation model for each time increment as properties of the gas flow were updated. The Klyachko drag equation is represented as:

$$C_D = \frac{24}{Re_p} \left(1 + \frac{(Re_p)^{2/3}}{6} \right), \quad \frac{\alpha_3}{\alpha_1 + \alpha_3} \leq 0.08 \quad (3-5)$$

where Re_p is the particle Reynolds number assuming an incompressible flow due to the relative insensitivity at low pressures of shear tensor in calculation of the Reynolds number. The particle Reynolds number values were obtained using the Chinook hydrocode described in Dunbar et al. (2011). The drag model used was an incompressible correlation for Reynolds numbers less than 1000 (Saito et al. 2003). Gas sound speed was initially fixed in the Mach number with an estimated molecular viscosity in the Reynolds number. With adjustments to the sound speed, recalculation of the model estimated low relative velocity, low Mach numbers, and low Reynolds numbers. This indicated that the drag model used was appropriate to the flow regime.

A diffusion particle burn model (diameter squared law) was used in the simulations assuming the mean PSD did not change from each of the starting materials. This approach assumes that the kinetics is faster than diffusion for the particle sized that was used.

Particle Concentration Estimates

Values for the numerical particle velocity and concentration at the FOV are provided with the Chinook code in an explicit time stepping method (Chinook manual 2006). A series of four steps and three progressive mesh remappings are solved in sequential steps. Particles and fluid continua are modeled and tracked using a two-phase Eulerian solver during the initial detonation and dispersal period known as the profile step. Later at the conversion step, 9-10 μs using the conversion solver the particle masses are converted by the Lagrangian solver using the known PSD of the initial powder. During the next step, in the intermediate domain, particle groups are modeled and “mapped” into a larger domain allowing mesh resolution to be decreased. In the final full domain the resolution is again reduced to decrease mapping errors. This is the point at which the data for particle concentration was extracted. The domain size and mesh resolutions used for each of the four steps are found in Table 3-2.

Estimating particle concentration in PIV images can be labor intensive. A method identified by Stitou et al. (2006) in conjunction with the PIV software was used. An electronically generated grid with interrogation regions set at 64x64 pixels was overlaid on to each particle field image. Each of the 64x64 interrogation regions were numbered and those with no particle images in the outer edge of the particle flow were masked out and not used in the concentration calculation to prevent skewing of the particle density. Several numbered regions were selected at random and the valid images counted in each region. The sum of the particle images within each region was then divided by the area of its region. All region values were then summed. The relationship for concentration is:

$$C_m = \sum_{i=1}^{N_d} \frac{N d_i}{S_{w_i}} \quad (3-6)$$

where C_m is the particle concentration, S_w is the area of the interrogation region and N_d is the number of particles counted within the interrogation region.

Shock Induced Momentum Transfer

Whether momentum transfer from a shock wave can result in an increase in particle velocity was evaluated using the equations identified by Zhang et al. (2003) for solid particle and gas shock interaction. The duration of time when the particle and shock are in contact is the shock interaction time, described as:

$$\tau = \frac{d_p}{D_0} \quad (3-4)$$

where d_p is the particle diameter and D_0 is the shock velocity. For the response time of particles, the velocity relaxation term is:

$$\tau_v = \frac{4d_p^2 \rho_t}{3\mu C_D Re} \quad (3-5)$$

and μ is the fluid dynamic viscosity. The ratio of these two terms, the shock interaction time over the velocity relaxation time, provides a criterion to determine whether the shock will transfer sufficient energy to the particle to make a negligible change in increasing the particles velocity. Zhang et al. (2003) stated that “in liquid explosive with aluminum particles of 0.1-1 μm , the shock interaction time is about the same order of magnitude or one order of magnitude smaller than the relaxation time.” Therefore the particle could be accelerated from the shock front (Zhang et al. 2003). These principles should apply to the particles in the gas phase as well as in the condensed phase but the particles would be subject to a much weaker shock as the

distance from the explosive to the particle increases. Additionally, the particle sizes of concern in this study are considerably larger and would be less affected by an air shock.

Results

The most profound differences in the particle patterns and velocities were observed between the different charge series. Early time expansion pattern differences at 50 μ s can be seen of the powdered aluminum in Figure 3-2a,b compared to the tungsten powder in Figure 3-2c and solid aluminum shell baseline in Figure 3-2d. Frame data from the HSFC images showed different particle front expansion rates with the smaller aluminum particles being the quickest accelerated and the tungsten powder (W-27) being the slowest (Figure 3-3). Early acceleration of the particle front not provided in Figure 3-3 identifies the rapid acceleration of H-10 contrasted to the much slower acceleration of the tungsten W-27 powder. A listing of charge configurations, mean experimental velocities and numerically estimated velocities using the Chinook model are provided in Table 3-3. The images also clearly show greater luminescence with the H-10 which has a larger quantity of smaller particles. These observations are in good agreement with Frost et al. (2002) in which magnesium spherical particles in a spherical or cylindrical charge case was used with sensitized nitromethane. Frost et al. (2002) determined that for a given charge diameter, if the charge size is large enough and ignition occurs, the smaller the particle size the more prompt the ignition and the greater the luminosity. For comparison purposes, the high melting point of tungsten at 3422 °C provides a stark contrast to the reactive soft aluminum material which has a melting point of 660 °C. The PIV particle images were clear and sharp with luminescence blocking the center most portion of some particle fields. Images of burning and broken particle were identified at higher magnifications. With tungsten,

there was an absence of luminescence from burning particles; however radiant energy from the hot particles was present other notable differences included absence of particle structures and a relatively well distributed particle field with little or no agglomerated particles.

The average mass of the aluminum solid shells were 4.5% less than the H-10, and 19.0% less than the H-95 powder charges. The mass differences in the powder charges were due to the differences in the PSDs and the resulting packing densities. The tungsten charge was as much as 8.8 times greater in mass than the aluminum solid shell case charge due primarily to its greater material density of 19.3 g/cc verses an aluminum density of 2.7 g/cc and its narrower PSD. A wider PSD allows for small particles to fit between the larger ones, resulting in a greater packing density per charge for the same material types.

The effect of mesh resolution sensitivity was investigated for the H-95 model with the parameters described in Table 3-4. Numerical results obtained using the two mesh resolutions indicated that the resolution has a large impact on fluid pressures (shock thickness), where as particle velocities are not significantly influenced. Both the coarse and fine resolution models used the same mesh for the profile and conversion steps. The intermediate mesh was not used in the coarse resolution model. In the full domain, the coarse and fine resolution models used the same cell size in a 2 m x 1.5 m region centered on the charge, however the cell size growth outside of this region varies.

Analysis

Image Processing

No post processing of the PIV images to reduce luminescence was required to improve the total number of good image pairs for the tungsten powder charges.

Background subtraction for the aluminum powder charges were needed to enhance the particle images due to luminescence. This procedure eliminated some of the false images in the deep field and reduced the low intensity ghost images from particles outside of the light sheet. The image enhancement process entailed an estimate of background luminosity from each frame; the value determined from each frame was then subtracted from the entire frame to proportionally reduce the luminosity across the entire frame. The use of advanced PIV image processing was necessary during vector processing of the aluminum powders and the solid aluminum shell charge fragments to track non spherical images. For the aluminum powders, though most retained their spherical shape, many did not and the formations of agglomerates and larger structures added complexity to the particle field.

The most effective grid engine processor used in this study proved to be a combined use of Deformation grid and the Deformation mask with the Hart correlation engine. This combination provided the maximum number of good vectors through greater measurement accuracy in complex flows. The Gaussian peak engine was used to locate the correlation peak. Post-processing used a global and local validation processor and vector field conditioning setup when recursive hole filling was needed. Mean particle velocity sensitivity with and without recursive hole filling values were compared on all velocity analysis and was shown in most cases to not differ more than 5%. The use of a processing mask reduced the effect of smoothing the mean velocity value by reducing the number of interpolated vectors for those cases where recursive hole filling was needed. A universal median test was used for local validation to remove bad vectors; it is an improved median filter which is a more robust validation method

than the mean because it is less sensitive to the flow field. Vector field conditioning used the local median for filling holes in the interrogation regions which failed validation.

The vector analysis settings differed slightly from each image set and from each powder series in order to maximize the percentage of good vectors. In uniform displacement fields it has been shown by (Adrian 1988; Westerweel 2000b) that the width of the displacement and correlation peak is proportional to the particle diameter (Westerweel 2000), this is why matching the peak algorithm to the correlation algorithm is important. Proper conditioning of the image spots before processing can reduce in and out of plane errors.

Lost images fell in three categories: 1) particle images lost from in and out of plane motion within the FOV 2) images which were lost from high background luminosity; or; 3) those lost within dense image structures where the individual particle images or a significant portion of their edges could not be determined. These types of losses are common in blast wave imaging due to the sudden acceleration, heating, material type, and projected solid angle influence of the curved charge surface at increasing radial distances.

Particle Velocity and Concentration

For comparison purposes the particle concentration can be based on valid images rounded to a whole particle, for H-10 the experimental determined particle number was not able to be established because of the large amount of clumping and overlapping of the individual particle images. For the H-95 experimental data, the average number of valid images in the FOV was determined to be 5.9×10^5 giving 12 particles per mm^3 in the FOV for W-27 the average number of particles was 6.1×10^5 or 12 particles per mm^3 . In contrast the simulation generated the average number of particles in the FOV to be

706 (9 particles per 1000 mm³), 9.10×10^5 (11 particles per mm³), 2.85×10^4 (4 particles per 10 mm³) for H-95, H-10 and W-27 respectively. Particle concentration determination by image count is subject to significant error if the valid image count associated with vectors and the frame image count from valid and non-valid images differ significantly.

For the solid shell, 1,948 particles were tracked experimentally by the PIV in the FOV, but only three were tracked in the FOV in the simulation. Two important differences in the solid aluminum shell experimental and simulation comparison were the arrival times at 1 m and the particle breakup model used in the simulation. The numerical image at 0.95 ms showed three particles within the FOV with an average velocity of 668 m/s. This is a 23% greater velocity than the PIV value. The difference in the time interval values between the experimental and numerical model can be explained from the breakup and drag model used by the simulation. The simulation model for this research used an Eulerian solver to simulate the initial expansion of the metal case in a fluid phase; this fluid is later converted to fragments after reaching a specified failure strain. At this point the fragments dispersal is simulated using the Lagrangian solver. Application of the drag equation numerical models was based on spherical metal fragments; a particle distribution with a 1 mm mean diameter was used because no data was available on the solid case PSD. This provided a representation that was significantly different from the experimental condition with the produced large irregular fragments. Calculations from the HSFC indicate the fragment arrival time to be 0.848 ms compared to the simulation time of 0.533 ms. This relates to an experimental

particle velocity of 1.5 km/s and a numerical predicted velocity of 1.8 km/s or a 300 m/s difference in velocity, hence different arrival times at 1 m.

A complete distribution of fragments was not recovered from the solid shell and for those fragments that were recovered many had large aspect ratios with dimensions of as much as 30 mm long by 4 mm wide. Clearly the numeric model deviated from the small spherical particle conditions imposed on the PSD in both mass and shape resulting in significant error between the experimental and numerical values. From Equation 1, differences in the experimental particle drag due to the irregular shape and increased area of the fragments becomes the dominate force for a later experimental arrival time at the FOV. For all of the powder charges the PSD was known and was utilized in the simulation models. Results from the numerical model compared favorably with the powder experimental values listed in Table 3-3.

Early Time Powder Front Velocities

A comparison of the particle front velocity for the aluminum and tungsten powders at early time showed a significant difference among the charges. The H-10 aluminum powder has good linearity in velocity after 50 μ s seen in Figure 3-3 from its quick acceleration by the fluid. The plots show that as the particle mean PSD increases, the particle front velocity decreases and later becomes nearly constant after its initial acceleration period. This is in agreement with predictions from Engelhardt (2006), Cooper (1997), Frost et al. (2005) and Dunbar et al. (2011) for spherical metallic particles of different sizes. The exception is W-27, with higher density and small particle diameter, the material is not accelerated as rapidly as the less dense aluminum particles of the same size and therefore attains a lower percentage of the gas velocity.

After its initial acceleration, W-27 velocity decreases more slowly than the other powders outside of the gas envelope and at 1 m it has a higher velocity than any of the aluminum powders (Table 3-3). Tungsten powder is about seven times the density of aluminum, thus the tungsten powder provides additional confinement with a greater transfer of energy to the particle shell. This may result in the expanding product gas seeking the weakest point of least confinement and an asymmetric early time fluctuation of the leading edge of the particle field. This can lead to error measurements as time progresses with the leading edge of the expanding particle field as variations along the particle front form and in some locations diminish; making it challenging to identify a representative particle front position from frame to frame.

The less dense particles of aluminum accelerate more quickly and approach equilibrium sooner with the high velocity product gas behind the shock; hence, they achieve a higher dispersal velocity. Some very small low density powders like H-10 have a large quantity of very small powder sizes below the mean which can be quickly accelerated by the initial shock and product gas expansion. This effect can be seen in the PIV image of Figure 3-4, set at 35.6 cm from the charge surface where the small material is accelerated ahead of the bulk material.

The aluminum solid shell fragments continue at high velocity beyond the time period shown in Figure 3-3 because of their greater mass and stored energy. Their higher stored energy comes from the greater pressure volume (PV) work of the product gases due to the added confinement of the shell prior to breakup. Because of the greater fragment masses, the inertia effects require a longer acceleration period to attain their maximum velocity and a longer deceleration at 1.0 m means higher

velocities at the FOV of 512 m/s than for the small particles, larger leading fragments are estimated via displacement and timing from the HSFC to be 1539 m/s.

For the experimental hand calculations, fragments from the solid shells were modeled with a projected area of a rectangle for estimating the drag coefficient. Many of the fragments had large length to width ratios and were imaged in early time shortly after case breakup. The size distribution that is imaged is contrary to the simulation model which is described as a normal distribution with a mean particle size of one millimeter. This was later shown to affect the differences between the experimental and numerical arrival times, velocities and number concentration at the FOV.

Error measurement grew with increasing time for each system tested. The irregular shape of the leading edge increased as the powders expand; for the solid particles the size, shape and ordination vary enough to significantly change their leading edge from frame to frame due to the particles rotational velocity. This caused the solid particle fragments to blur and made it difficult to identify a defined edge as can be seen in the Figure 3-14 HSFC image.

Particle, Fireball and Shock Interaction

As has been seen in the PIV images for all of the aluminum powder systems, structures of agglomerated particles existed within the blast wave. These structures vary somewhat in character depending on several factors including the initial PSD, total mass of the particle bed, the bed packing density and thickness. The agglomerations in the structures are a combination of induced agglomeration due to shock at early time and particle heating and burning from the intrusion of product gases into the particle bed. Broken particle fragments were also identified in the PIV imagery at higher magnification, Tanguay et al. (2007) stated that his numeric simulations indicating that

particles underwent severe plastic deformation and failure. Changes in gas flow were numerically simulated by Ling et al. (2009) under limited conditions of a shock tube by studying the propagations of disturbance waves generated by the particles in the expansion fan. It was concluded that disturbance waves produced by the movement of the particle laden field changes the gas flow in the expansion fan resulting in the preceding shock wave to decelerate. This suggests that the influence of particle laden expansions are apt to decrease the intensity of the formation of complex shock structures and shock induced heating ahead of the particle field than those shocks ahead of a pure gas flow. This may partially support the explanation for the broadening of the H-10 particle field of greater particle concentration in Figure 3-11 as compared to the H-95 particle field in Figure 3-12. Additionally, the work reported by Eaton and Fessler (1994) suggests that structure formation or lack of them in random regions and dissipation of these flows could be linked to turbulence.

The greatest opportunity for particle, fireball and shock interaction occurs at early time (0-10 μ s) with the primary shock and intrusion of hot product gases occur within the particle bed prior to the cardboard shell splitting. Velocity and temperature transmission factors described by Ripley (2007) and momentum transfer to solid particles by Milne (2000) and Zhang et al. (2003) provide the mechanism for agglomeration at early time. Simulations describing particle and shock position in early and later time for each of the powder series are provided in Figure 3-5, 3-8.

For H-10 the first early time crossover of the shock wave and particle field occurred at 0.09 ms and 0.18 m (Figure 3-5a). Calculations of the ratio of the shock interaction time to the velocity relaxation time gave a value of 6.72E-4. The shock

interaction time value is 3 orders of magnitude smaller than the velocity relaxation time (Table 3-5). Thus from Zhang et al. (2003) the particle crosses the shock front with negligible changes in its velocity. Temperature of the air just behind the shock was determined from the Normal shock tables (Anderson 1997) to be 1740 K. The second H-10 shock interaction showed a smaller ratio also providing a negligible momentum transfer with the air temperature behind the shock of 834 K. In Fig 3-5b, it can be seen that the shock front velocity becomes linear which is representative of a sonic wave. Therefore, although the particle velocity did not significantly increase, energy would be transferred to the surrounding environment as heated air.

The H-95 had only one crossover point with the particle front and shock wave at 0.11 ms and 0.22 m (Figure 3-6a), with a shocked air temperature of 763 K. The shock interaction time to the velocity relaxation time ratio was $9.73E-5$. The shock interaction time was 4 orders of magnitude smaller than the velocity relaxation time suggesting that the shock would not significantly affect the particle velocity (Zhang et al. 2003). The tungsten powder had one particle and shock crossing point due to its slow particle field velocity (Figure 3-7a) at 0.24 m and 0.19 ms, the inertness of the tungsten and later PIV imagery indicate no material change occurred. Interaction was possible after the passage of the primary shock front from the H.E. reactive wave when the powder was packed in the particle bed, it has been reported by Richards et al. (2004) that the PSD of tungsten powder used in condense explosives changed and that deformation of the particles can be observed.

A comparison of all the powder series plots shows that shock and powder interactions available to form agglomerates took place during the initial particle shock up

and expansion or before 0.15 ms. For H-10 the PIV image of Figure 3-4 was taken at 2.5 ms, with close inspection this image shows signs that agglomerated structures have already formed and that some very small material is ahead of the main particle cloud. From the simulation plots of Figure 3-5, 3-8 the 2.5 ms time is earlier than the second particle and shock crossover periods for H-10, implying that the second intersection of the two crossovers is not the primary event in forming the agglomerations. Additionally, the linear shock line in later time indicates a constant velocity which is consistent with a low energy acoustic wave incapable of containing enough energy to preheat the region between the shock and the particle front. For H-95, the particle front does not cross the shock front a second time within the 5.7 ms period. The first and only crossing point in Figure 3-6a occurs at 0.11 ms, and 0.22 m which is at a greater distance away from the charge surface than for the H-10 crossovers points. This provides for additional time for adiabatic cooling during the expansion period, reducing the temperature to 763 K. In addition, for the H-10 powder, the simulations show first crossovers of the shock and powder fronts between 80 and 100 μ s, earlier than for H-95 and less opportunity for cooling. During the period between 20-120 μ s, the HSFC powder images showed developing combustion in the particle front which would provide an opportunity for the hot particles to be forced together and agglomerate.

For the powder series the zone just behind the shock at the first powder shock cross over point the air is at a high temperature because it is shock compressed. This zone also has a higher oxygen concentration than ambient and provides an additional opportunity for particle heating and burning, thereby, promoting additional agglomeration. Images in Figure 3-2 at 50 μ s show a lessening of combustion as

particle size increases. A decrease in aluminum particle combustion as the diameter increases has also been reported by Zhang, (2005) for aluminum and Frost et al. (2005) for magnesium particles.

Simulations identified that changing inert particles to reactive particles causes the speed of both the particles and the shock front to increase. As the particles burn the particles decrease in size. Smaller particles accelerate faster and approach equilibrium with the high velocity gas behind the shock and thus achieve a higher dispersal velocity. Also, as they burn they release energy to the fluid causing the shock speed to increase.

The W-27 in contrast to the reactive aluminum with its high melting point and greater hardness produced no agglomeration or particle structure formation seen at one meter. Its high density resulted in slow acceleration with high inertial properties leading to a higher velocity than the other powder charges in the PIV FOV. Simulation results revealed an average drag coefficient for the W-27 powder that is lower than for the aluminum powders at 5.7 ms with a measured experimental velocity of 50.5 m/s. The solid shell shock and large fragment simulation cross over point occurs at about 0.10 ms at 0.19 m.

Particle Velocity Gradient within the Particle Field

From twelve PIV images of H-95 charges, velocity analysis was conducted on three horizontal band regions within each imaged particle field. The bands were positioned at the same location in the FOV for every one of the twelve frame pairs. This provided velocity data at distinct locations within the FOV, enabling a mean velocity and standard deviation for each band to be determined. Figure 3-9a is a representation of the approximate location of the three velocity band regions. From Figure 3-9b it can be seen that the mean particle velocity is slowest at the top of the FOV in Band 1 and

fastest at the bottom of the FOV in Band 3. In Band 2 the mean velocity was lower than for Band 1 or Band 3. The standard deviation was greater in Band 2 than for Band 1 or Band 3, indicating that the range of velocities were greater than in the other bands. In Band 2 a higher percentages of negative velocities were measured by the PIV analysis software indicating directional changes and turbulent mixing.

Experimental Reproducibility

Considerable importance was placed on the ability to demonstrate repeatability of the measured velocity values from the particle fields generated by the test charges. Twelve H-95 powder and six H-10 charges were produced, screened and tested under identical conditions and placed at the same relative position as described previously. After processing the images and generating a velocity contour plot of the shot, the mean velocity values were imported into a statistical process control software package (Petrovich 2007).

Figure 3-10a for H-95 and Figure 3-10b for H-10 show that the velocity means of each experiment falls within two standard deviations of the mean value. For the determination of the vector distribution normality, the combined 42,228 vectors from the twelve H-95 shots were used. A normal distribution with a mean of 7.75 m/s and a standard deviation of 0.84 m/s was calculated. A vector count of 7,563 from six of the H-10 shots were also determined to have a normal plot, with a mean of 5.79 m/s and a standard deviation of 1.38 m/s. Both data sets passed the normality tests in the statistical package using the Anderson-Darling, Shapiro-Wilk and Lin-Mudholkaria criteria for a normal distribution of velocities. Both charts indicate a random fluctuation about the mean. This met the standard criteria for an in control process which can be repeated. Although the H-10 series had only 6 independent tests, their similarity with H-

95 in construction, testing and the thousands of vectors which passed the normal distribution tests indicate a process that is in control and can therefore be qualified as a repeatable process.

Conclusions

This research demonstrated success in imaging and determining velocity values of small metallic particles driven by the product gas of an explosive using HSFC and PIV instruments. PIV is limited to particles that can be fully illuminated by the lightsheet, any particles larger than the thickness of the lightsheet can't have their size or velocities measured accurately. Estimates of fragment velocity can be estimated by determining time of arrival and its displacement from the source.

Imaging the different particle materials showed a stark difference in characteristics between aluminum powders of different sizes and a tungsten powder. Due to shock compression and heating at early time and aerodynamic attraction possibly due to turbulent effects, large image dense particle structures were produced by the aluminum powders. Tungsten powder, in contrast, was well distributed with little or no agglomeration and showed little luminosity with individual particles being generally less bright than aluminum particles. The images clearly show that changes in material type and the particle size can significantly affect the speed, agglomeration of particles and the particle structures within the flow field. The imagery also suggests that influences from large particle structures in highly dense particle flows, can produce characteristic large-scale structures like those reported and classified by Elghobashi, (1994) as four-way coupling. Wang and Maxey (1993) identified the importance of inertia bias from particles, especially heavy ones, with particles tending to collect into elongated sheets on the peripheries of local vortical structures. Simulation models like that of

Balakrishnan et al., (2010) in conjunction with experimental data can probe the dispersion of inert material and the shock attenuation by the particle gas mixture could also be helpful. The velocity gradient within the particle field provides an explanation for the lengthening of the particle field at increasing distances from the source. This phenomenon provides a natural separation method of the particles with greater inertia.

Additionally, a method to determine the drag coefficients for the different particle fields using two velocity values was demonstrated with results comparing well with the numerical model results. This provided confidence that the simulation model has the ability to provide usable comparative data.

The combined imaging capability of HSFC and PIV can provided a practical method to aid in the validation of detailed model algorithms designed to investigate velocity, mixing and particle concentration for hydrodynamic codes such as Chinook and the CFD code Second-Order Hydrodynamic Automatic Mesh Refinement Code (SHAMRC). The accurate characterization of these phenomena is a significant effort and of high priority for complex blast models.

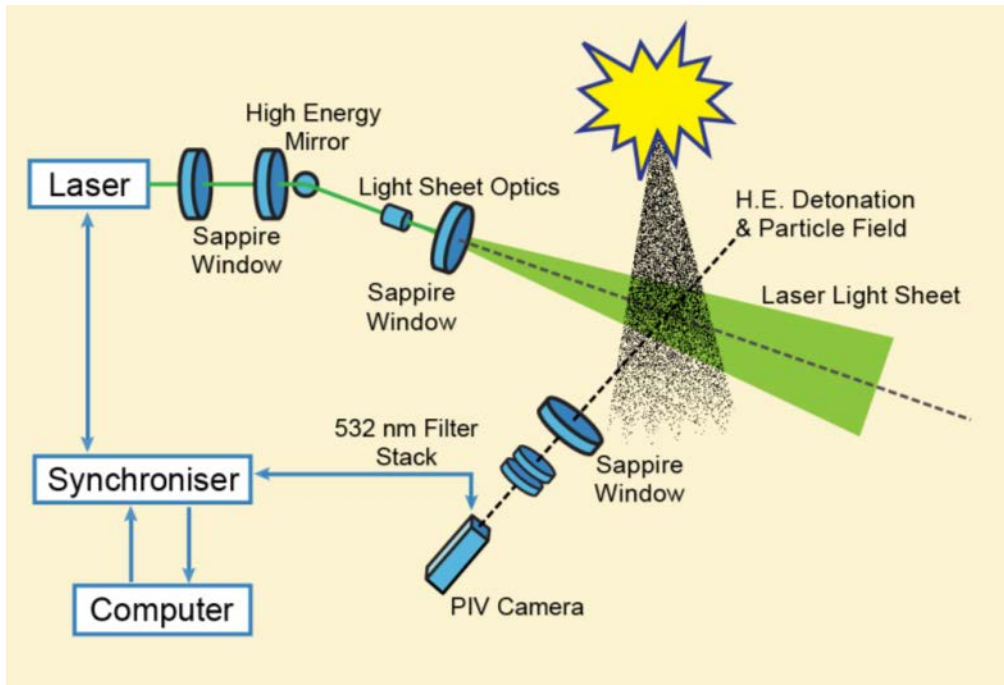


Figure 3-1. PIV test setup (view top down), high explosive was set above the light sheet with particle flow in a downward direction.

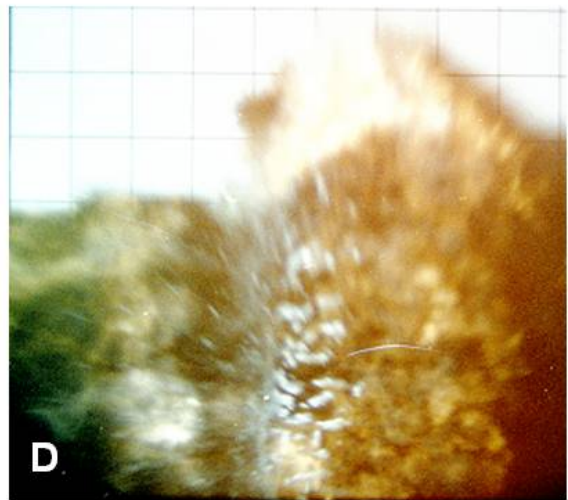
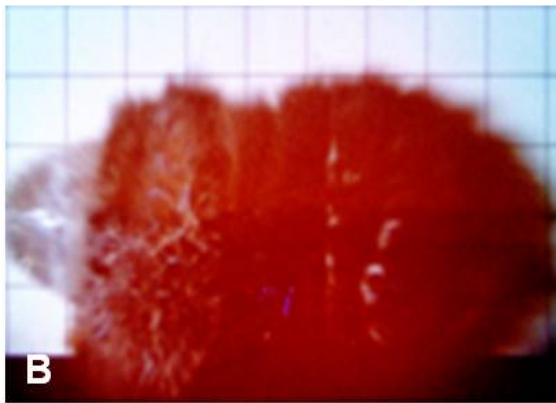
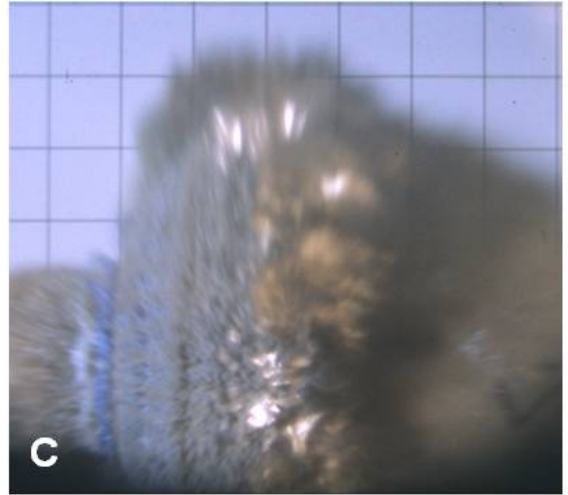
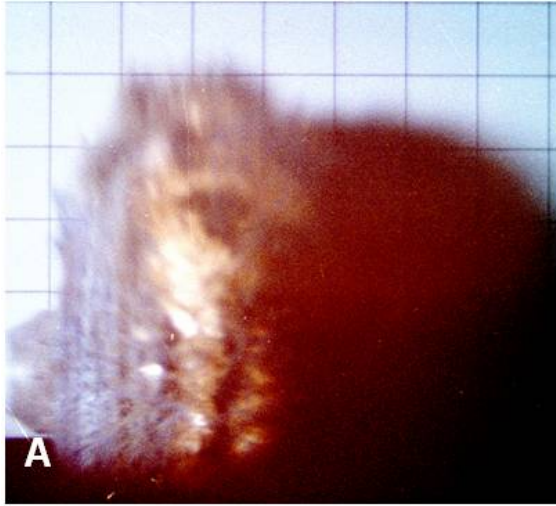


Figure 3-2. Early time expansion of powders and fragments imaged using the HSFC, all initiated at 50 μ s from the right end. A) An H-10 powder annulus charge (one inch per block) B) tungsten particle charge expansion, no combustion due to the inert metal powder, irregular shaped expansion C) H-95 powder annulus charge D) aluminum solid case breakup with fragment images at 50 μ s post detonation.

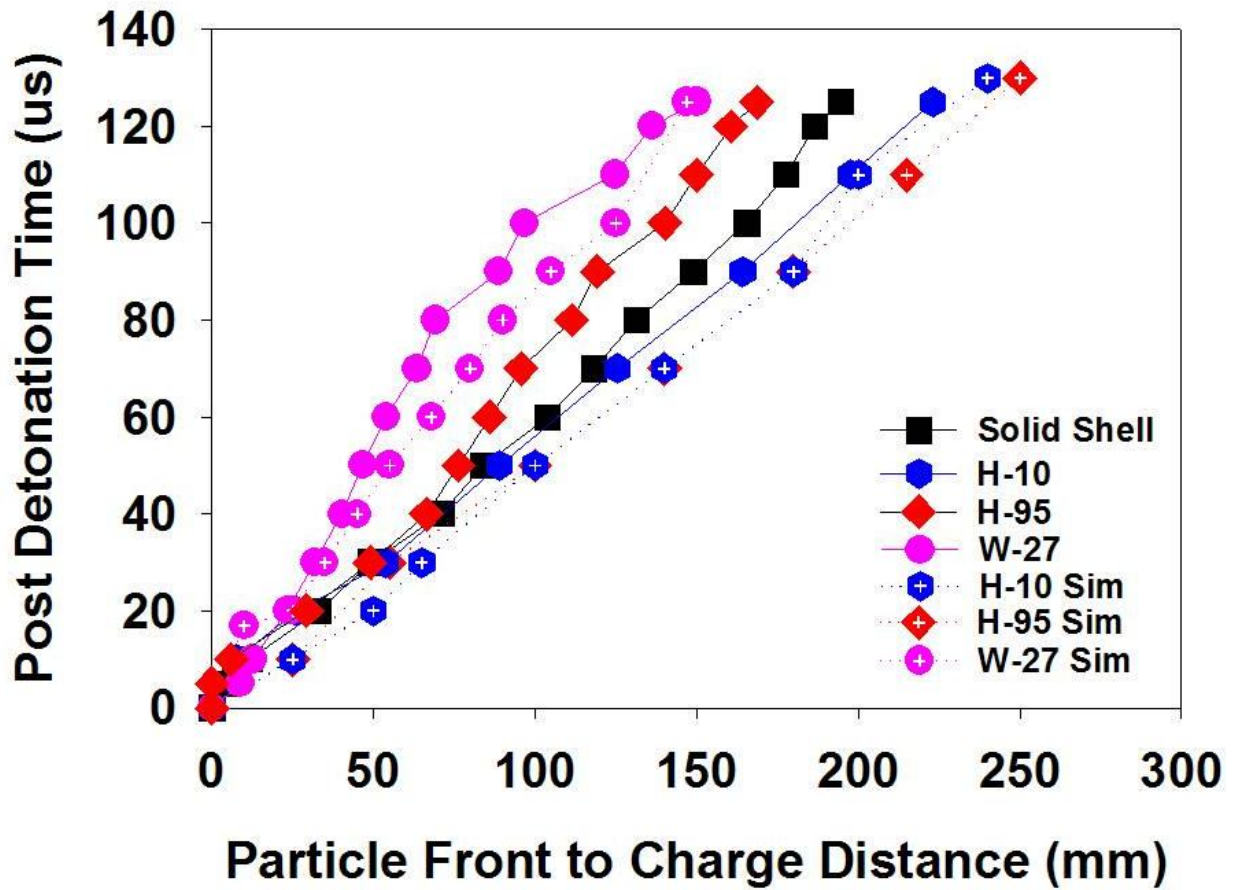


Figure 3-3. Early time experimental and numerical expansion data. The H-10 powder is linear after a quick acceleration in the first 30 μs . W-27 can clearly be seen lagging in the early acceleration and slowly continuing past 125 μs . Error bars are smaller than data point figures. Closer examination of the first 10 μs , not shown, shows slower acceleration of the W-27 material.

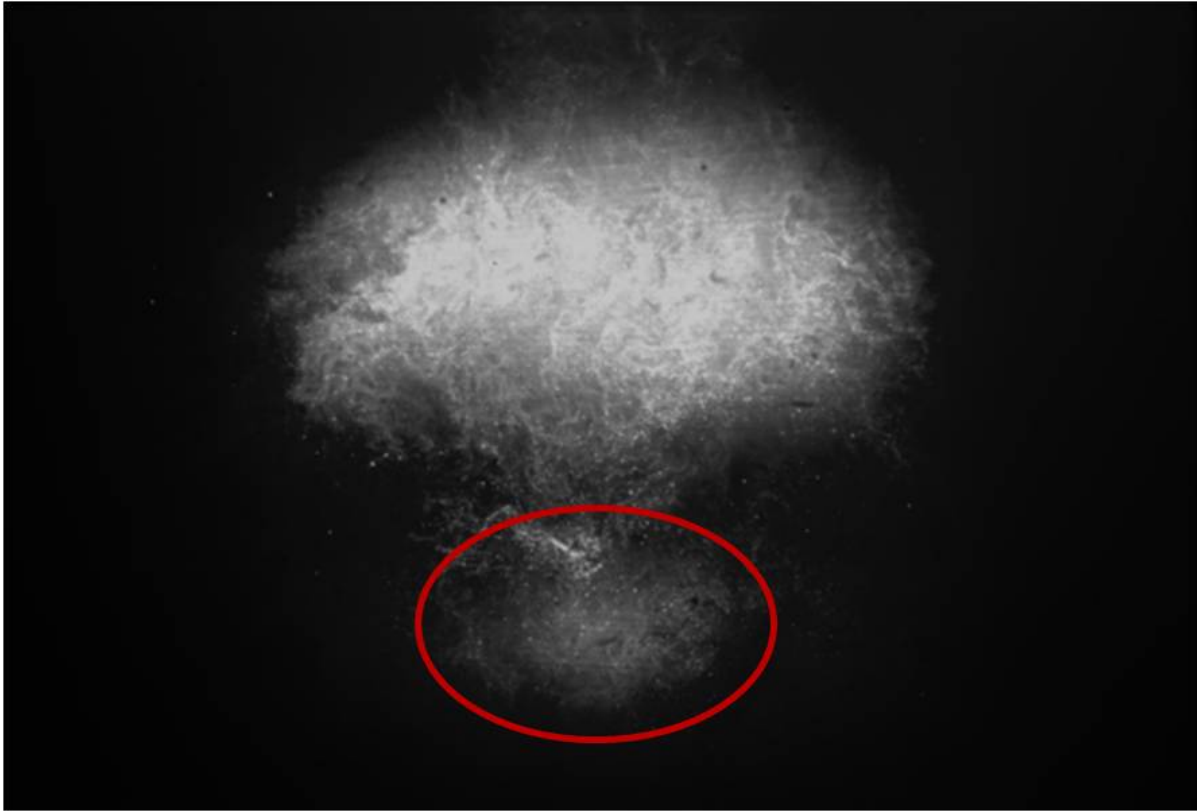
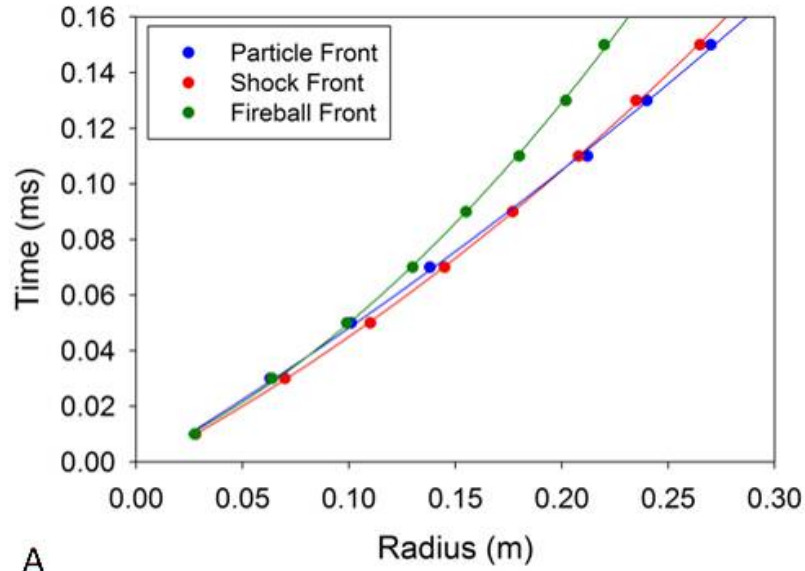
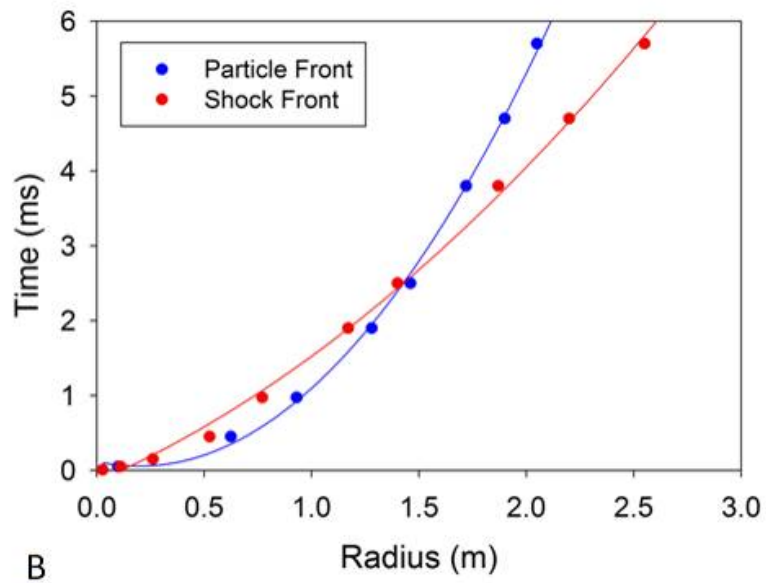


Figure 3-4. H-10 particle fields moving from top to bottom, at 44.7 cm from charge surface, 2.5 ms post detonation. A small particle cloud (in red) ahead of the main particle body may be due to acceleration of very small particles to near gas velocity. Upon close inspection some threads or regions of high particle content can be seen to be forming within the cloud.

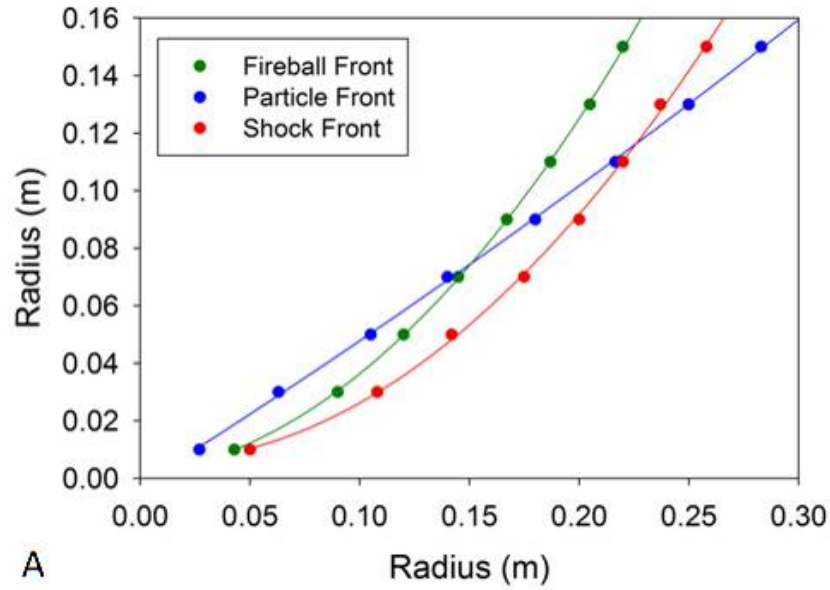


A

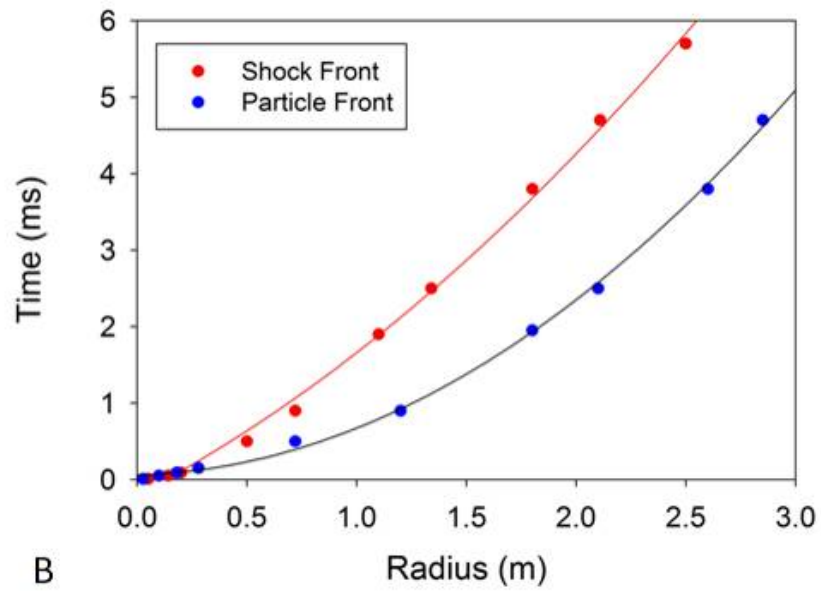


B

Figure 3-5. Particle and shock front trajectory for the HMX explosive surrounded by 23.1 g of H-10, A) $t = 0 - 0.15$ ms, B) full simulation $t = 0 - 2.5$ ms.



A



B

Figure 3-6. Particle and shock front trajectory. A) for the HMX explosive surrounded by 26.3 g of H-95, 0-0.15 ms, B) full simulation $t = 0 - 2.5$ ms.

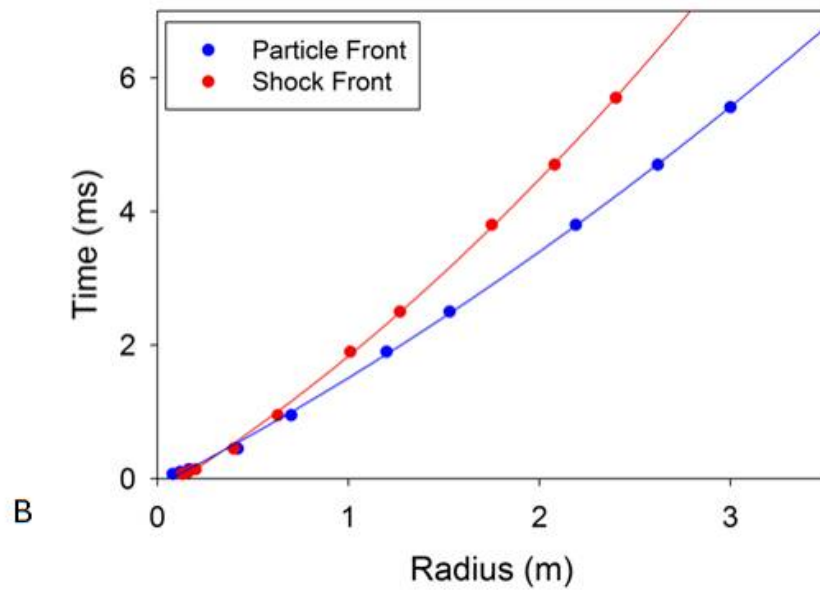
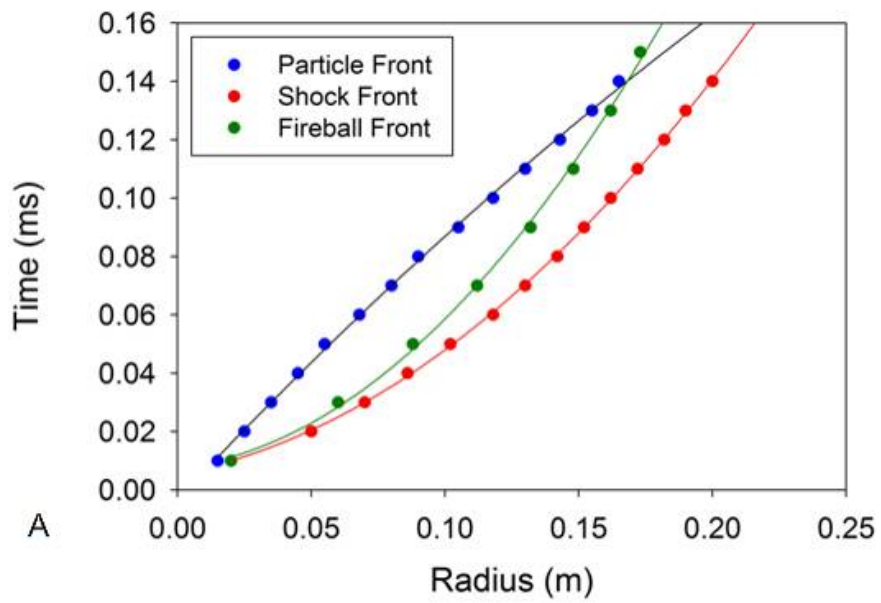


Figure 3-7. Particle and shock front trajectory. A) for the HMX explosive surrounded by 215.8 g of W-27, 0-0.15 ms B) full simulation t = 0 – 5.7 ms.

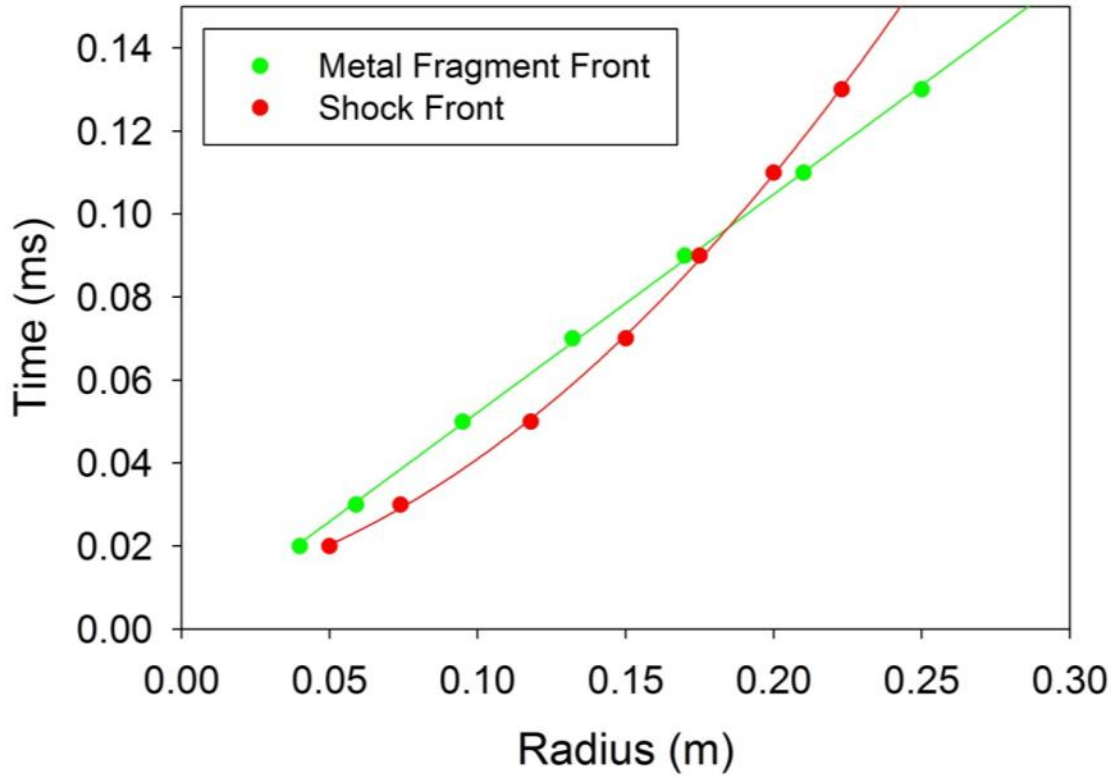


Figure 3-8. Fragment and shock velocity plots for a 22.1 g solid aluminum case, 0-0.15 ms.

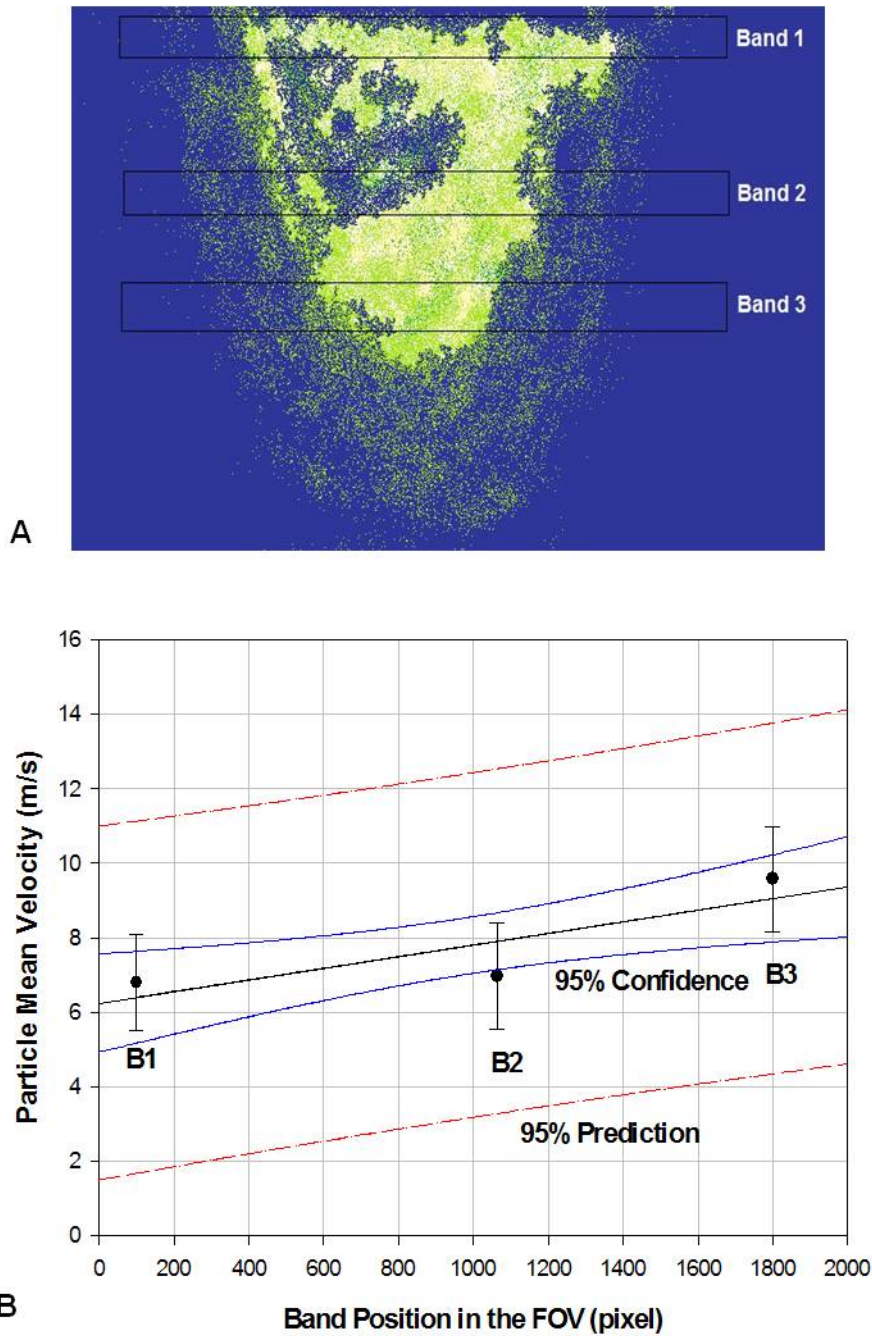


Figure 3-9. Representation of a PIV image A) band zones displayed from which a particle velocity gradient was established, B) Particle band mean velocity values from the H-95 powder series.

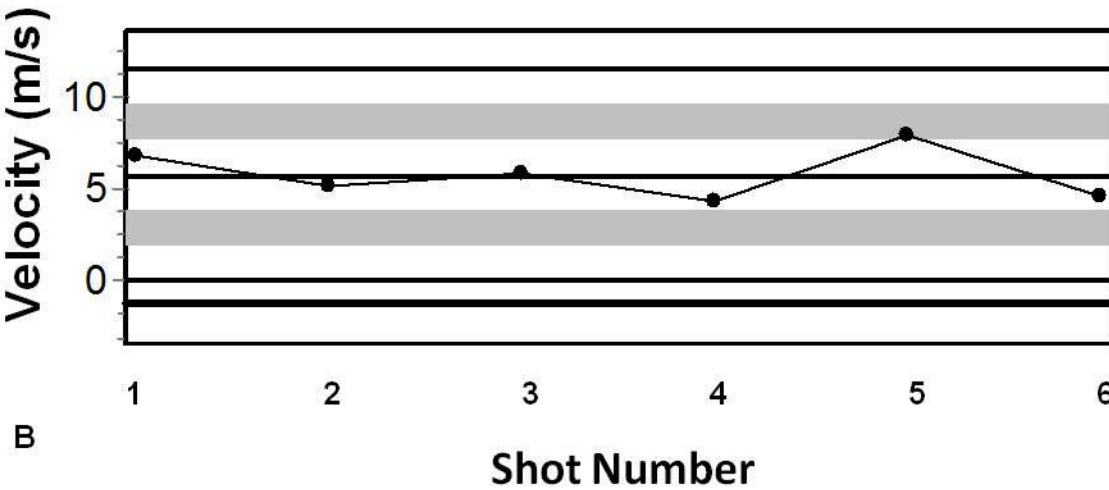
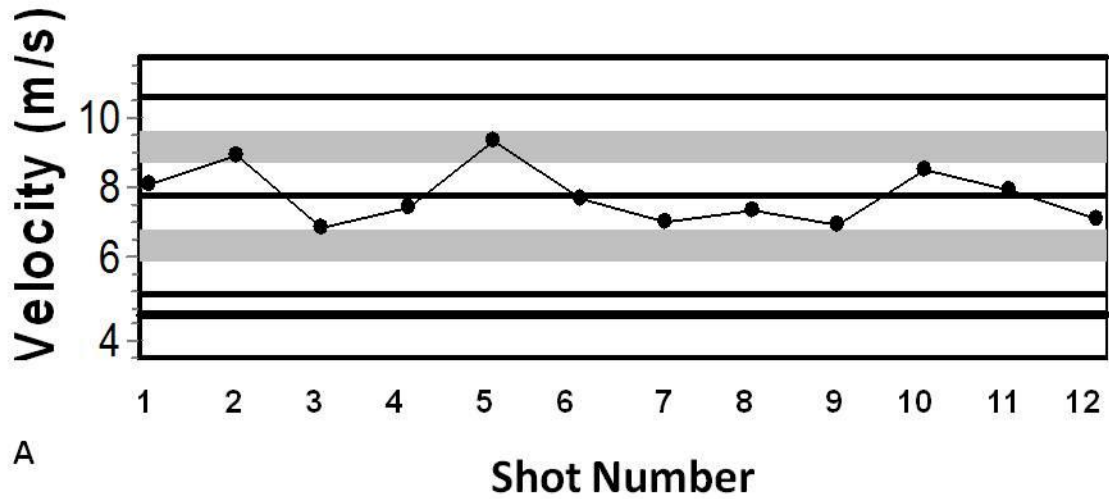


Figure 3-10. Mean particle velocity vs. shot number. A) as measured H-95 experimental mean particle velocities of the image pair for each of 12 test shots. Mean velocity of all shots is 7.75 ± 0.84 m/s within the FOV, B) As measured H-10 experimental mean particle velocities of each image pair for vectors calculated within the FOV. Mean velocity of all shots is 5.79 ± 1.38 m/s within the FOV.

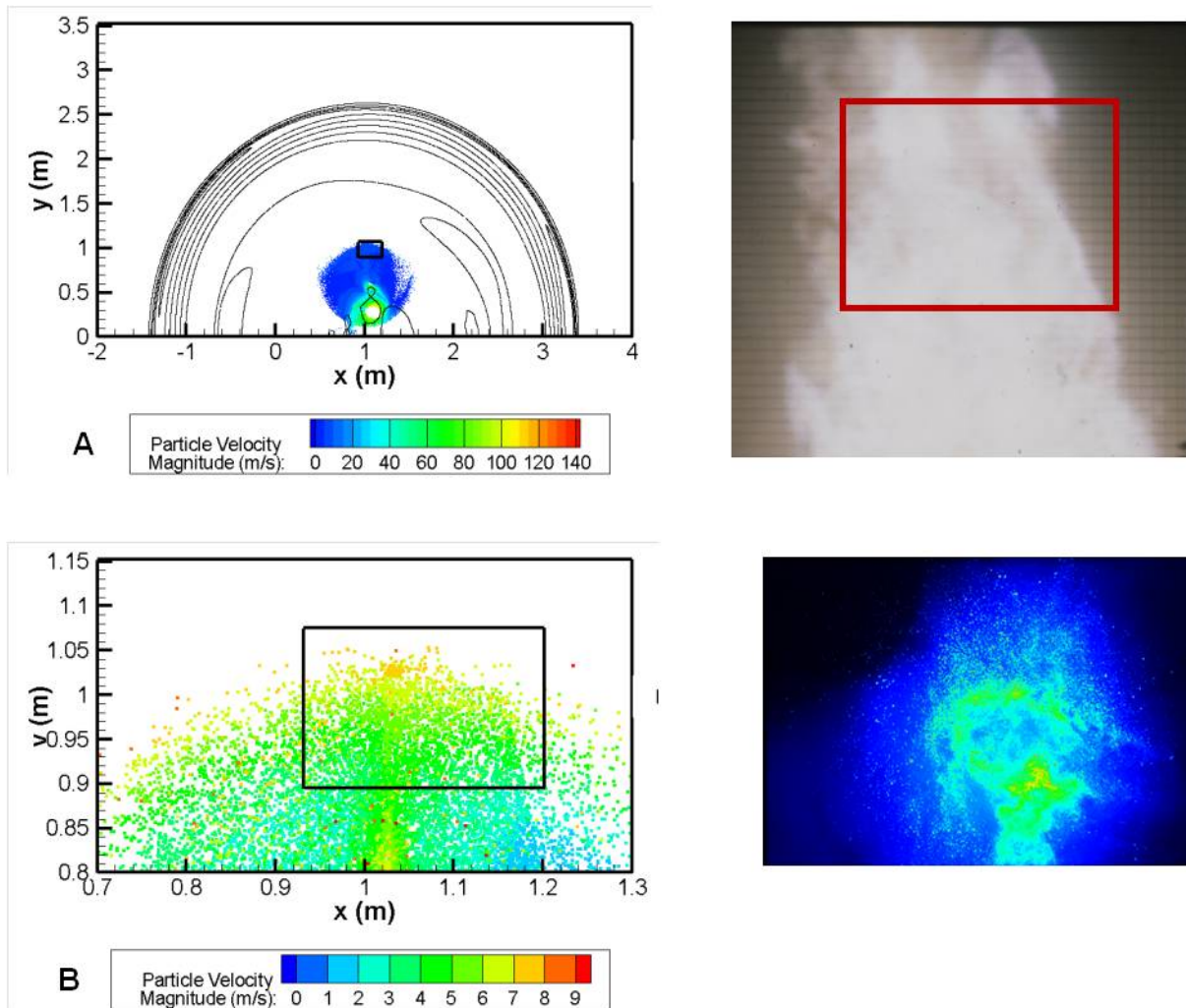


Figure 3-11. Composite of H-10 simulation, visual and laser images at 5.7 ms. A) Particle dispersal simulation for HMX charge surrounded by 23.1 g of H-10; right, visual image from HSFC, estimated position of PIV image within red box, B) Close-up of particle tracking window in (skip every 5th particle group), with a numerical mean velocity of 5.50 m/s right, raw PIV image cropped to remove empty image space. HSFC grid is in cm.

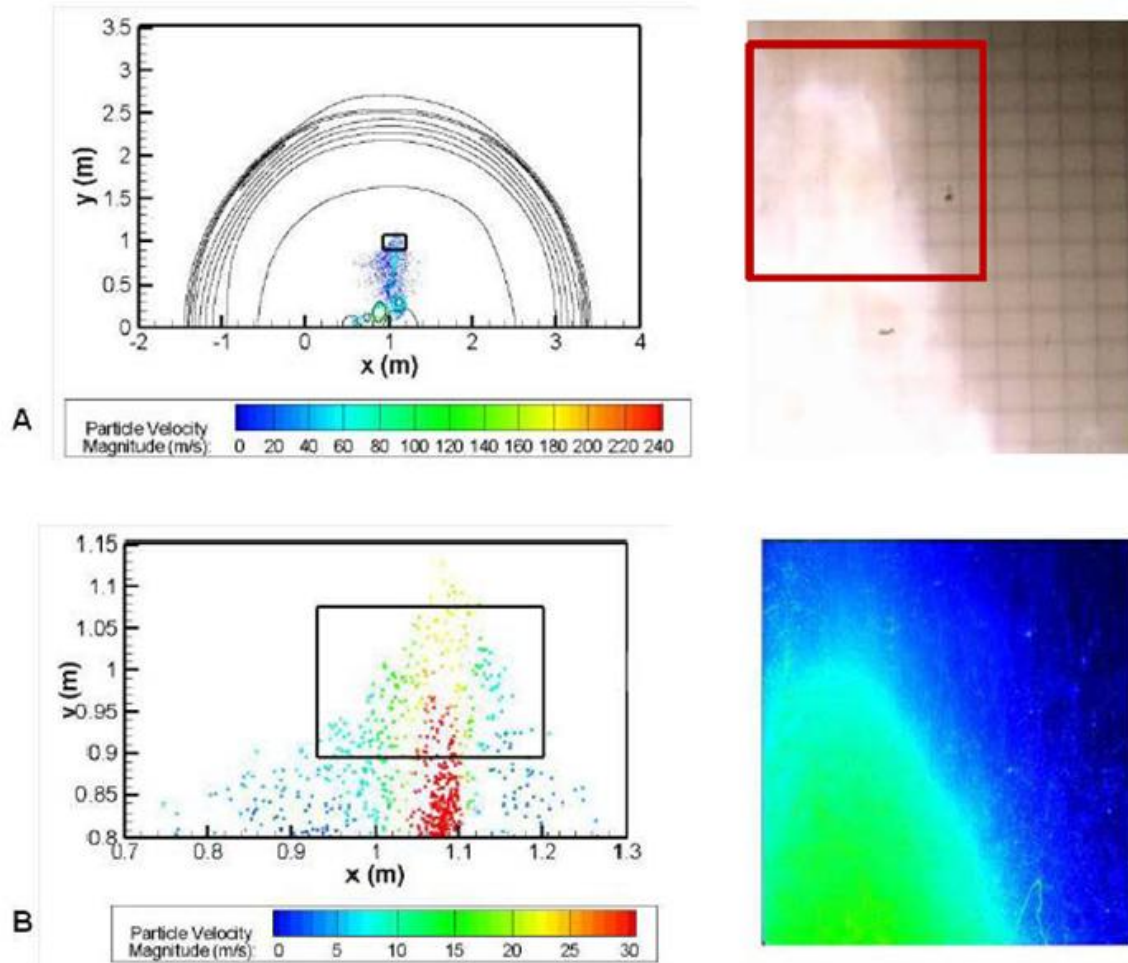


Figure 3-12. Composite of H-95 simulation, visual and laser images at 5.7 ms. A) Particle dispersal simulation for HMX charge with 29.8 g of H-95; right, visual image from HSFC, estimated position of PIV image within red box, B) Close-up of particle tracking window (assuming small particle counts cannot be visualized), with a numerical mean velocity of 13.20 m/s, right, raw PIV image, slight off center due to particle drift as seen in HSFC image, cropped to remove excess empty space on the right. HSFC grid is in inches.

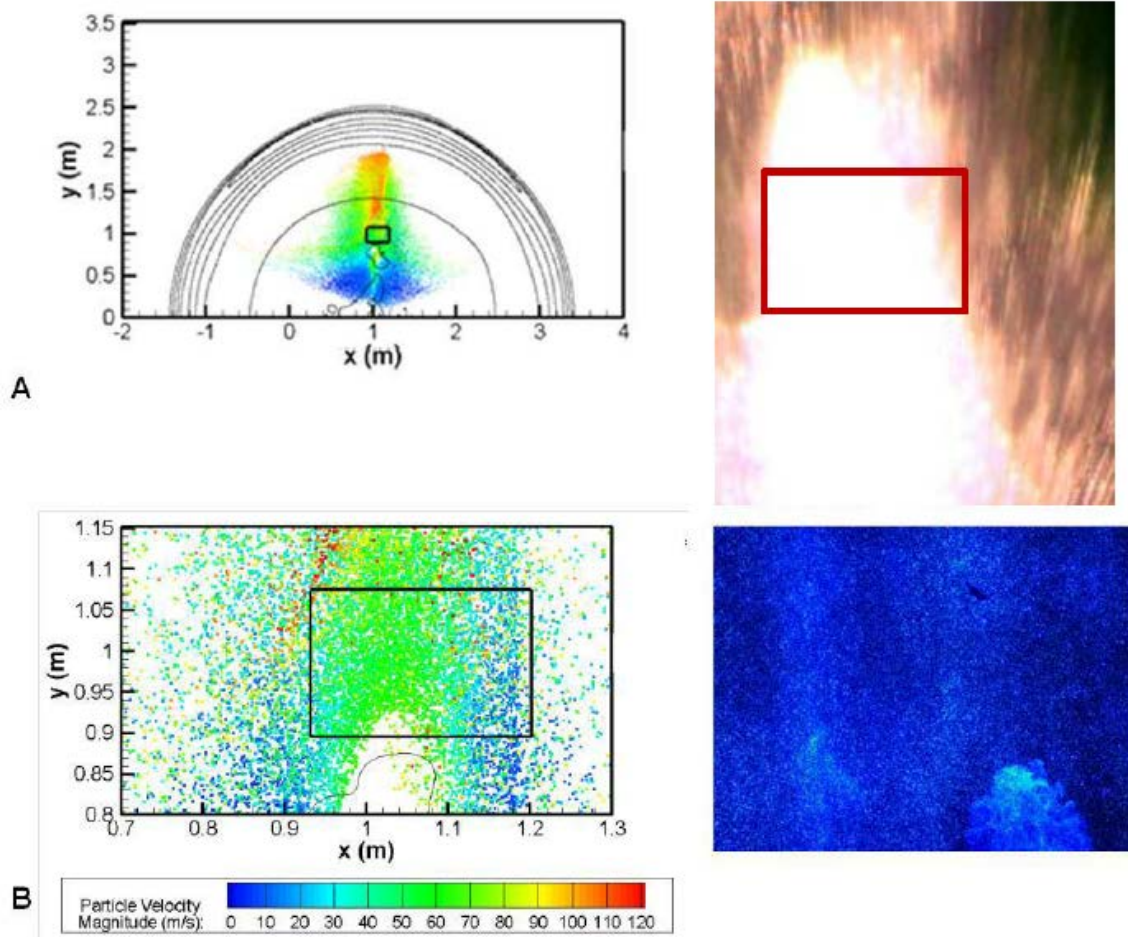


Figure 3-13. Composite of W-27 simulation, visual and laser images at 5.7 ms. A) Particle dispersal for W-27 HMX; right, HSFC image with estimated FOV position boxed in red, B) Close-up of particle tracking window (bottom, skip every 5th particle), with a mean numerical velocity of 55.3 m/s right, full PIV image of FOV.

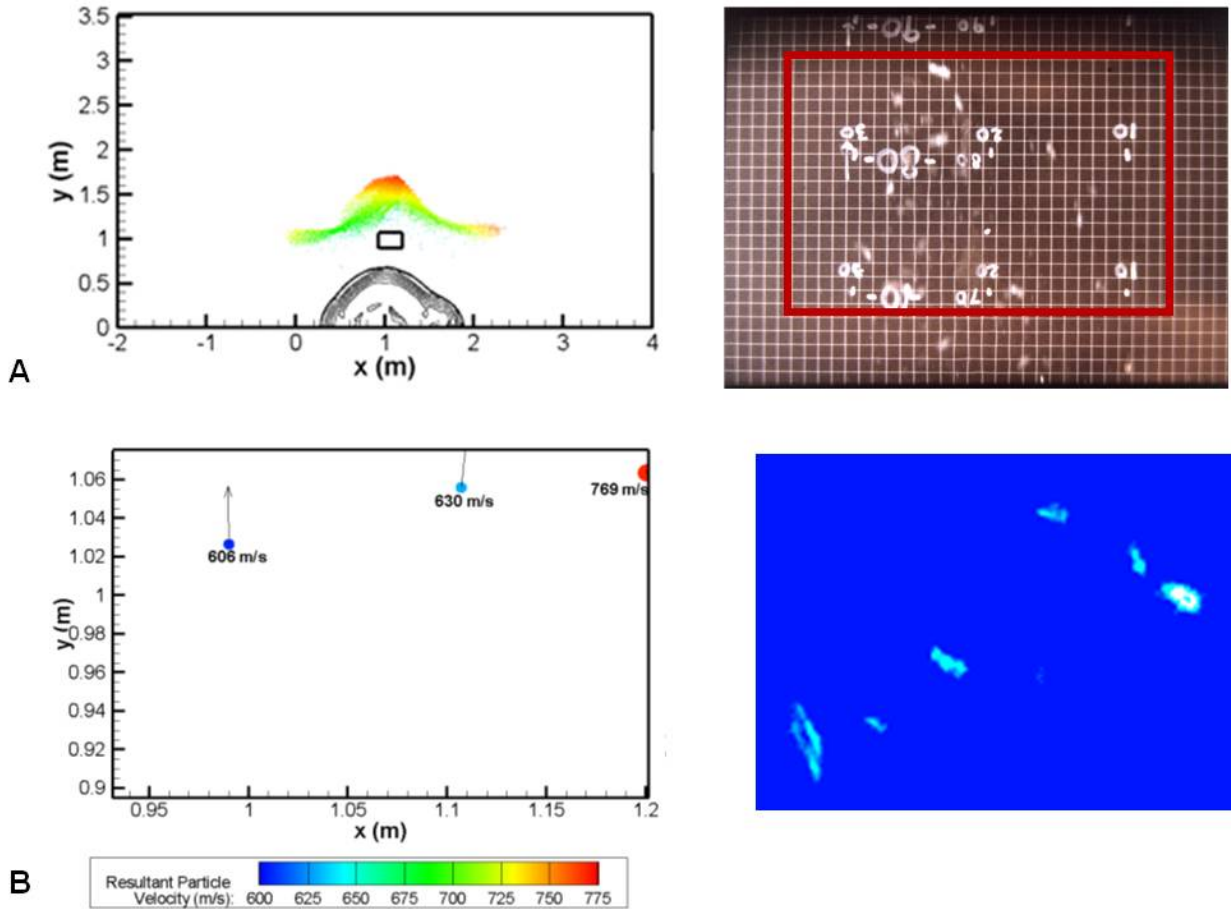


Figure 3-14. Composite of solid case particle simulation, visual and laser images. A) Simulation of fragment velocity at 0.95 ms for a 22.1 g solid aluminum casing. Motion is upwards to top of the frame, leading metal fragments have a prescribed distribution with $V_p = 1.6$ km/s; right, visual image of fragments, using HSFC $V_p = 1.2$ km/s at 1 m for large fragments, HSFC grid is in cm B) close-up simulation view within the FOV, right, raw PIV image cropped to fit space and magnified, because full size image was mostly empty space with small fragment images in the FOV. Differences in fragment reflectance are primarily due to angularity and orientation of particle.

Table 3-1. Charge mass properties

Charge Type	Average Annular Powder Mass (g)	Average Tap Density (g/cc)	Average Total Charge Mass (g)
Aluminum Powder (2.70 g/cc)			
H-10	23.10	1.60	53.98
H-95	26.30	1.82	56.65
Thick solid shell (3.2 mm)	22.10	na	32.60
Tungsten Powder (19.3 g/cc)			
W-27	215.80	14.90	241.80

Table 3-2. Mesh resolution for PIV dispersion simulation

	Mesh type (cell type)	Domain size (mm)	Mesh Resolution (mm)	End Time (ms)
Step 1. Profile	quadrilateral	150 x 50	0.1	10 x E-3
Step 2. Conversion	quadrilateral	150 x 50	0.1	10 x E-3
Step 3. Interim. Mesh	triangular	950 x 350	0.8	0.150
Step 4. Full Domain	triangular	6000 x 3500	3.0 - 150	5.7

Table 3-3. Experimental HSFC, PIV and numeric velocity values

Charge Type	Exp. Early Time Velocity (Km/s)	Numerical Velocity (Km/s)	Exp. PIV Velocity (m/s)	Numerical Velocity (m/s)
Aluminum				
H-10	1.53	1.75	5.79	6.10
H-95	1.32	1.78	7.75	16.6
Solid Al shell	1.69	1.90	512.0	668.0
Tungsten				
W-27	1.29	0.80	50.5	55.3

Table 3-4. Mesh resolution sensitivity study

	Mesh Shape	Domain Size (mm)	Mesh: Coarse Resolution (mm)	Mesh: Fine Resolution (mm)
Step 1. Profile	quadrilateral	150 x 50	0.1	0.1
Step 2. Conversion	quadrilateral	150 x 50	0.1	0.1
Step 3. Interim. Mesh	triangular	950 x 350	Not used	0.8
Step 4. Full Domain	triangular	6000 x 3500	3.0 - 150	3.0 - 6.0

Table 3-5. Experimental and simulation derived drag coefficients with shock velocity interaction time ratio

Charge Type	Experimental Average Drag Coefficient	Simulation Instant. Drag Coefficient	Ratio of Shock Interaction Time to Velocity Interaction Time at crossover points $\left(\frac{\tau}{\tau_v}\right)$
Aluminum			
H-10	0.36	1.08*, 6.97**	6.72E-4
H-95	1.93	0.86*, 8.25**	9.73E-5
Solid Al Shell	0.36	NA	NA
Tungsten			
W-27	2.46	0.87*, 6.51**	NA

* Values are determined at 1.0 meter

** Values are determined at 0.44 meter

CHAPTER 4
IN VITRO DISSOLUTION AND SIMULATION STUDIES OF ALUMINUM POWDER
USED IN HIGH EXPLOSIVE AND REACTIVE MIXTURES

Introduction

Aluminum is a low density metal that when mixed as a small diameter powder, roughly ($50\text{nm} < x < 100\mu\text{m}$) with a high explosive (HE) provides stored chemical energy in the form of a fuel which is used to provide additional energy for the blast wave. Small sizes are being investigated because of their high surface to volume ratio, providing the opportunity for higher reaction rates compared to larger material of the same type. Aluminum powder has been used in high explosive formulations for both the military and industrial applications for many years since it became commercially available. Exposure to workers from small aerosolized powder during the HE manufacturing process is possible because of the ease with which the material can be suspended with simple mechanical action. For very heavily laden aluminized explosives, particularly those configurations with a particle bed surrounding the high explosive, unburned particles were identified in the work conducted in Chapter 3 using particle image velocimetry. Additionally, fractured particles have been reported in simulations and in the post detonation particle size distribution of hard refractory powders such as tungsten by numerical simulations (Ripley et al. 2006) and by experimental methods from Richards et al. (2004). In either case, the resulting aerosolized cloud has a wide range of particle size distributions (PSDs) even within the nano range (Cheng & Jenkins 2005). Researchers and technicians exposed to the particle cloud can incur an inhalation hazard if personal protective equipment such as a high efficiency filter mask or respirator is not used. The exposure level to different PSDs may vary greatly

depending on the performance and the mechanical property of the bulk solid and the configuration of the HE.

The dynamic environment of the evolving particle cloud and the physical activity of the individual can provide an exposure that will affect the rate, amount and location of deposition within the different locations in the lung. The time-dependent variation of extended exposure affects the quantity of the material dispersed to the different organ compartments. For this study the production and inhalation of nano-material in the 1, 10 and 100 nm range was of primary interest with the exposure data provided by the results from the research of Cheng & Jenkins (2004). This size region is of particular interest to researchers because of the ease by which the material can become aerosolized during handling operations and the difficulty of conducting research without specialized containment equipment.

Exposure and deposition computational models such as the Integrate Modules for Bioassay Analysis (IMBA) can under specific criteria provide estimates of the amount of material inhaled and initially deposited in the lungs along the various extrathoracic and thoracic respiratory airways. Furthermore, clearance models within IMBA provide for time-dependent translocation of inhaled material to blood, lymphatic nodes, and the gastrointestinal tract. Once in the blood, systemic biokinetic models within IMBA provide for time-dependent uptake, retention, and washout of materials within all potential source organs and tissues. Instantaneous lung fluid clearance rates determined by either ICRP default values or by direct experiment can support the effort to determine estimates of material concentrations in the organs such as the lungs, blood, spleen, liver and mineral bones (ICRP Publication 66, 1994). While specifically

designed for radioactive aerosol exposures, the models and code structure of IMBA can accommodate non-radioactive aerosols inhalation scenarios with proper adjustment to remove in situ radioactive decay of the material. The ICRP has consistently recommended that, material specific absorption parameter values, obtained preferably from in vivo data, or alternately from in vitro dissolution experiments, should be given preference over ICRP default values for exposure/dosimetry calculations (Ansoborlo et al. 1999). In vitro dissolution techniques provide a simple, cost-effective method by which lung fluid dissolution rates for particles can be estimated and have been utilized as a screening method to classify default solubility categories in situations where in vivo dissolution data is not available (Ansoborlo et al. 1999).

Once the dissolution rate constant for the powder was determined, the rate constant was adjusted by multiplying its value by the ratio of the adjusted weighted volume mean particle moment $D[4,3]_1$ divided by the original weighted volume mean particle moment $D[4,3]$ determined from the starting particle PSD. This approach is similar to the method Tinke et al. (2005) used for determining the average rate constant of multimodal particle systems from the sum of the products of the individual rate constants and their volume mean particle size moments.

The default values for relatively insoluble materials are listed in the ICRP Publication 66 Human Respiratory Tract model as either fast, medium, or slow (Type F, M, or S, respectively) with each having a different clearance rate $\lambda(t)$. The ICRP currently recommended GI-tract, tissue dosimetry, biokinetic, and bioassay models and provided them in IMBA, to standardize internal dose assessments. The IMBA simulation program allows for user input of numerous model parameters in order to

calculate an estimated intake and/or dose (James & Birchwall 2003) using default or supplied parameters.

Materials and Methods

The static dissolution method used in this research and the artificial lung fluid identified as Serum Ultrafiltrate (SUF) simulant is consistent with the Lovelace Respiratory Research Institute (LRRI) system described by Ansoborlo et al. (1999). A method similar described by Sdraulig et al. (2008) for dissolution of uranium mining samples and beryllium powders accomplished by Stefaniak et al. (2006) was used in this research.

Aluminum powder for the dissolution experiment was provided by Valimet Inc., the material was designated as H-2 and is one of several materials from their spherical powder series. A mean particle diameter of $3.87 \pm 1.93 \mu\text{m}$ was determined using a Beckman Coulter LS 13320 laser diffraction particle sizer in addition to its geometric standard deviation, the PSD, and the volume-weighted mean particle moments. Additional powder characterization was conducted by imaging of the particles with a scanning electron microscopy (SEM) for particle size, shape and extent of agglomeration (Figure 4-1).

Preparation of the aliquot samples for determination of metal concentration was done using an ICP/MS (model 7500) made by Agilent. The ICP instrument required the samples to be diluted 10:1 to maximize its accuracy and reduce the corrosion effects of the high salt content in the solvent. The dilution liquid was distilled de-ionized water with an yttrium standard; the yttrium standard provided the means to calibrate the conversion of the number of counts detected by the ICP/MS to the amount of metal ion solute per unit of solvent (mg/l) read as parts per million (PPM).

A spread sheet was devised to adjust for slight mass differences in the initial sample and to the concentration values for each calculation of the rate constant at each time interval. An average of the twelve sample concentrations was determined for the average rate constant. The concentration data provided the determination of the mass removed which was subsequently subtracted from the initial mass. The fraction remaining over the initial mass of the sample (M_t/M_0) was then calculated and plotted versus time in hours; a dissolution curve was then produced using the best fit equation. The data points were plotted with error bars based on the two standard deviations. The equation for the best fit of the data was determined to be a single exponential equation based on the R^2 value from single and double exponentials. Once the best fit equation was determined, the instantaneous clearance rate to blood λ (t) and the average dissolution rate constant were then calculated.

Solvent Preparation

The preparation of SUF stimulant was conducted in accordance with an internal developed standard operating procedure (SOP) in compliance with LRRRI published requirements as adapted from various procedures derived from the literature, primarily from the work conducted by Eidson et al. (1990), Ansoborlo et al. (1998) and Stefaniak et al. (2005). The solvent was mixed in accordance to an accepted formula in ten liter batches and held for no longer than 30 days in a darkened cabinet. The finished solution was corrected to 7.3 ± 1 pH prior to use. The chemical formulation for SUF used in this research is listed in Table 4-1.

Dissolution

An image of the dissolution system is shown in Figure 4-2. The system used twelve 1 liter polycarbonate containers, each filled to 750 ml with SUF. The jars were

made by Nalgene, containing a slightly modified 47 mm in-line polycarbonate filter holder made by Pall Corporation (Figure 4-3). The modified filter holder had slots cut in the rim of the filter support and in the retaining ring to allow air bubbles to be removed from under the filter membrane. This design helped to prevent trapped air bubbles from damaging the membrane while also increasing the solvent contact surface on the membrane and sample powder surface. The filter holder was centered and the legs attached to the bottom of the dissolution cell with a silicone adhesive. After an overnight curing period, a Teflon coated stir bar was placed under the center of the filter holder to provide agitation of the solvent in the dissolution cell.

Continuous low speed stirring of the SUF solvent was used to reduce the concentration gradient and ensured uniformity of the solvent solution; this is a constraint in the dissolution model developed by Mercer (1976). The material sample was held in place by a sandwich of three membranes. The membrane sandwich consists of a 0.45 μm polycarbonate support membrane, made by Sterlitech, which sat atop the holder support screen, two additional 0.1 μm polycarbonate membranes containing a sample of the H-2 material held between them was placed on top. The membrane sandwich was then secured in place by the overlay of a plastic "O" ring while the upper section of the holder was gently tightened into place. A measured amount of SUF solvent fluid (750 ml) was carefully placed into the dissolution cell and the container lid was then secured; began time zero for the dissolution process. For the dissolution cells that were continually monitored by a pH probe, the probe was carefully inserted into the vessel through a port cut in the container lid. The probe was set to a mid-level depth as to not hit the filter holder or the bottom of the dissolution cell container. An additional port

fabricated on the opposite side of the pH port allowed for sampling via pipette without disturbing the dissolution cell and pH probe monitoring.

The dissolution cells were interconnected by a system of 3/16 inch ID Tygon tubing that delivered a gas mixture containing 5% CO₂ in N₂. The interconnecting tubing which delivered the gas was controlled and monitored by a mass metering instrument produced by Alltech Inc., designated as a Digital Flow Check HR. The tubing was of equal length to each dissolution cell with minimal bending to ensuring an equal pressure drop and therefore an equal mass of gas delivered from the supply cylinder to the cell. Quick-connect plastic fittings from Cole Parmer were used to allow easy disconnection from the gas supply line to the mass flow monitor and supply tank, an inline filter was placed between the mass flow meter and the supply tank to ensure no foreign debris made its way into the dissolution set-up. Measurements of the cell pH was done in the closed dissolution cell to reduce evaporation of the solvent, prevent contamination, stabilize metal concentrations, and ensured a consistent control of the solution pH. Without the stabilizing CO₂ gas, the pH value of the solvent rose quickly to a basic value as metal hydroxides were produced and the solvent hydrolyzed as described by Eidson (1990). A water bath of 37.0 ±0.1°C surrounded the dissolution cells and was maintained using an Isotemp bath heater made by Fisher. The water bath heater circulated a closed circuit of distilled water with a copper coils immersed in each of the three water bathes Figure 4-2 for heat transfer. Each water bath contained four dissolution cells in which the water was continuously circulated via a small water pump. This setup ensured that the proper temperature was maintained within the bath and dissolution cells during the dissolution process. Both the bath temperature and the

pH of at least one cell in each of the three water baths were monitored continuously during the dissolution process with intermittent pH checks of other cells using a mobile pH and temperature meter.

The drift towards a basic pH value was especially strong during the first two days of a new sample. This made it difficult to adjust the proper amount of CO₂ gas to the cells and required attention to each cell pH during the day and night hours with adjustment to the gas flow every couple of hours in the first two days. To monitor and support the control of the pH in each cell, a mobile Fisher Accumet pH probe was used in conjunction with the automatic temperature probes (ATP), the displays made by Orion. This method proved to be consistently successful at maintaining temperature and pH within the proper limits of each cell during the seven day dissolution process.

Mercer (1967) developed a dissolution theory for powders which is based on the mass fraction remaining from a single homogenous particle after a time period t, represented as:

$$\frac{M_r}{M_o} = \left[1 - \frac{\alpha_s kt}{3\alpha_v \rho D_o} \right]^3 \quad (4-1)$$

Where M_r is the sample particle mass remaining, M_o is the initial particle mass, α_s and α_v are the surface and volume shape factors, k is the dissolution rate constant, D_o is the initial physical particle diameter, ρ is the material density and t is the time period since the beginning of solvent contact with the sample. Mercer (1967) also expanded the theory to include mono and poly-distributed powders with specific criteria limiting the standard deviation of the PSD for single and double exponential particle system models.

Of the many different dissolution methods, the static method was used in this research because it has been proven to provide the ability to run many samples

concurrently while producing dissolution constants very similar to those produced from dynamic methods (Ansoborlo et al. 1999).

Assumptions governing the dissolution process include the necessity that the concentration of the dissolved solute is very low and that the dissolved solute does not have any effect on the rate of dissolution into the solvent. This is controlled by the amount of sample mass and volume of solvent used in each dissolution cell. Additional assumptions include that the mass transport film thickness surrounding each particle is uniform and consistent and does not vary with the change in particle size. This parameter is controlled by the even distribution of the sample on the membrane surface, ensuring that overlapping of the particles is minimized; homogeneous in their material structure and that the solvent homogeneity is controlled by constant stirring to prevent solute concentration gradients.

Stefaniak et al. (2006) simplified the process and analysis by imposing initial criteria on the Mercer's equations. This was done by forcing the powder samples to become statistically monodistributed by using a five stage cyclone particle separator to produce a powder sample with a geometric standard deviation of no greater than unity ($\sigma_g = 1.0$) and a β less than 1.5. The poly-distributed particle system is described as having a β term for a collection of the values, $(\alpha_s kt)/(3\alpha_v \rho D_m)$, where the initial particle diameter D_o is replaced with the mass medium diameter D_m (Stefaniak et al. 2006). Additionally it has been shown that if the remaining mass fraction (M_r/M_o) is limited to values greater than 0.3, that greater control over the particle size distribution during dissolution is possible where the transition in particle population shape is more likely maintained. These limiting criteria provide the boundary conditions that allow for a

simplified single exponential term to characterize the dissolution results from of poly-distributed PSDs. The simplified powder system allows the equation to become:

$$\frac{M_r}{M_o} = \exp \left\{ -\lambda k t S S A \exp - \frac{\sigma^2}{2} \right\} \quad (4-2)$$

where, $\lambda = 1.18$, k = dissolution rate constant $\left(\frac{\text{mass}}{\text{area} * \text{time}} \right)$, t = time, SSA is the specific surface area $\left(\frac{\text{area}}{\text{mass}} \right)$ at time zero determined by surface adsorption of a helium monolayer by weak van der Waals attraction (Brunanuer et al. 1938). The standard deviation in the particle size distribution is $\sigma=0.5$ ($\sigma_g=1.0$). This relation can then be rearranged and solved for the average dissolution rate constant (\bar{k}_e) for the particle material;

$$\bar{k}_e = \frac{-\ln\left(\frac{M_r}{M_o}\right)}{1.04 S S A t} \quad (4-3)$$

Tinke et al., (2005) demonstrated an numerical approach to determine the average dissolution rate constants \bar{k}_e with a non-normal multimodal distributed PSD using the volume moment weighed mean diameter $D[p,q]$ (volume moment) of each mode and summing the products of the rate constant times each multimodal volume moment weighed mean diameter of each mode. The volume moment weighed mean particle diameter was calculated as:

$$D[p, q] = \left[\frac{\sum_i n_i X_i^p}{\sum_i n_i X_i^q} \right]^{1/(p-q)}, \text{ with } p > q \quad (4-4)$$

where, X_i is the center size of a class and n_i is the number of particle per size class and for the volume moment weighed mean particle size $D[4,3]$ is used where $q = 3$ because of the volume measurement being three length values and $p = q+1$ because of

the mean value of length needed as the final term. By multiplying the ratio of the volume weighed mean particle diameter $D[4,3]_1$ of the adjusted PSD over the $D[4,3]$ of the original PSD, a dissolution rate constant for the aluminum sample was determined.

In this study, the adjusted experimentally determined dissolution rate constant was compared to the ICRP lung fluid solubility default values using IMBA to assess remaining mass fractions within the respiratory tract and extra-pulmonary systemic organs of the body as a function of time post-exposure by inhalation. Number concentrations were used to calculate the mass inhaled for each particle size at six selected sampling times. A five minute inhalation exposure time at the breathing rate given for an adult male at light exercise ($1.5 \text{ m}^3/\text{h}$) was assumed (ICRP 1994) for the mass calculation. Inhalability was assumed to be 100 percent and the shape factor for the particles, assumed be spherical, were set to a value of 1.0.

The calculated inhaled mass values were used as a corresponding input value to the particle diameter for the IMBA code. Since IMBA treats only radioactive nuclides, aluminum-26 was used as the surrogate radionuclide in IMBA (physical half-life of 7.16×10^5 years); the simulation results were thus scaled by $e^{\lambda t}$ to remove the artificial effects of in-vivo radioactive decay. To model a mono-disperse particle size distribution in IMBA, the geometric standard deviation (GSD) was set to unity. The mass density of the particles was set to 3 g/cc rounding from the pure aluminum density of 2.7 g/cc. Moderate absorption to blood was assumed with the mass remaining in the whole body and lungs for each particle size at each selected sampling time calculated over a 30 day period. The remaining mass was then used to calculate the fractional mass remaining as a function of time.

Results and Discussion

After each sample period, concentration data was obtained and the rate constant was calculated using the removed mass over the initial mass relationship. As shown in Figure 4-4, a method using a single decaying exponential equation with nonlinear adjusted regression was used to find the best fit equation to the data. The best fit over all for the sampling times was provided by:

$$f(t) = y_0 + Ae^{-bt} \quad (4-5)$$

The calculated exponential coefficient (b) was determined to be $-\lambda = 0.0051$, which is similar to the default ICRP value for an intermediate rate of absorption into blood. Comparison of the fit to a single exponential yielded an adjusted $R^2 = 0.9955$ and a standard error of estimate of 10^{-4} . The single exponential fit passed all statistical tests including the Durbin-Watson test (2.3305), normality test ($p = 0.3534$) and the PRESS value of 0.0041. The PRESS indicates good predictive ability by the model, which is why a minimal PRESS value is desirable and usually indicates that the model is not overly sensitive to any single data point.

The fit with a double exponential was also attempted in the form of:

$$f(t) = y_0 + Ae^{-bt} + Ce^{-dt}$$

It provided an adjusted $R^2 = 0.9968$ and passed the normality test with a value of 0.5165 but the coefficient $A = 4.1275$ yielded a very high standard error of estimate of 2195 and very high standard error of estimate for the value of $C = -3.0786$ was 2196. The resulting coefficients for $b = 0.0089$ and $d = 0.0133$ were very large. The statistical tests showed failure for the Durbin-Watson test and a very high PRESS statistic of 10.2758 and a convergence of 73%. The selection was therefore made in favor of Eq.

4-5 as the best curve fit for this powder system. During the curve fitting process the differences between values were weighted based on a normal distribution, this provides a calculated data point that is more accurate at approximating the dissolution rate constant than just a simple averaging approach. Averages provide more weight to skewed values within the data set than a weighted approach assuming a normal distribution of the data.

By providing, for the proper conversions, the average experimental dissolution rate constant was calculated as:

$$\bar{k}_e = \frac{0.0051}{1.04 * SSA * t} = 3.53 \times 10^{-7} \text{ g/cm}^2 * \text{day} \quad (4-6)$$

where SSA is the specific surface area in g/m²-day and \bar{k}_e is the average rate constant in g/cm-day.

The volume weighted mean diameter from the original aluminum H-2 PSD was calculated as:

$$D[4,3] = \left[\frac{\sum_i n_i X_i^p}{\sum_i n_i X_i^q} \right]^{1/(4-3)} = 3.33 \quad (4-7)$$

The PSD of the volume weighted mean diameter for an aluminum PSD with a standard deviation of no greater than ($\sigma_g = 1.0$) about the mean (see Figure 4-5) using the original PSD was determined to be:

$$D[4,3]_1 = \left[\frac{\sum_i n_i X_i^p}{\sum_i n_i X_i^q} \right]^{1/(4-3)} = 2.83 \quad (4-8)$$

The ratio of the two moments provided a value of:

$$\frac{D[4,3]_1}{D[4,3]} = 0.850 \quad (4-9)$$

The value of the H-2 experimentally determined rate constant using Eq.4-3 and the ratio of the volume weighted means for the adjusted H-2 PSDs (Eq. 4-9) now can provide the relation of the mass dissolved to the initial mass of powder using a single exponential described as:

$$\frac{M_d}{M_0} = (1 - e^{-D[4,3]_1/D[4,3]\bar{k}_e t}) \quad (4-10)$$

Where the corrected average rate constant for the moment adjusted experimental value is:

$$\bar{k}_c = D[4,3]_1/D[4,3]\bar{k}_e \quad (4-11)$$

The experimental and corrected rate constants and their moment ratios are listed in Table 4-2.

In Figures 6A to 6C, IMBA simulation results are shown for Type M aluminum giving the fraction inhaled aluminum remaining within the total body, as well as lungs, mineral bone, and other soft tissues, as a function of time post-intake for mono-disperse particles sizes of 1, 10, and 100 nm, respectively. For 1 nm Al particles shown in Figure 6A, the initial whole-body and lung retention upon acute inhalation is 98.7%, and thus only 1.3% of the aluminum mass is exhaled. The lung burden of aluminum is shown to fall rapidly over the first 5 days of exposure, with particle dissolution to blood, and rapid incorporation of systemic aluminum within the soft tissues and, to a lesser extent, mineral bone. At 10 days post-intake, the whole body retention is only 9.3% of the inhaled mass, with a distribution of 5.0% in the lungs, 3.0% in soft tissues, and 1.3% in mineral bone. At 30 days post-intake, these percentages are 2.9% in lungs, 2.8% in soft tissues, and 1.2% in mineral bone. Similar patterns are shown for inhalation of 10

and 100 nm aluminum particles, with a corresponding decrease in the initial lung burden due to greater deposition in the extrathoracic airways at these larger particle sizes.

Conclusion

The statistical tests conducted on the data and regression fit provided confidence that the samples followed a normal distribution from which the standard deviation calculation can be used as a measure of spread from the mean. It also validates the used of the Durbin-Watson test statistic from which it can be inferred that the time series regression model chosen is independent and is non-auto correlated. The high coefficient of determination, R^2 , offers insight as to a good measure of the fit by the single exponential model and variable selection while the PRESS value is a measure that the fitted values for the model can predict the observed response, which is why minimizing PRESS is desirable.

The remaining fractional mass of aluminum after inhalation exposure to nano particle material was reported using default ICRP absorption values. The majority of the remaining fraction was excreted within the first 4 to 5 days post exposure. On average, the 1nm particles had the lowest final remaining fraction for all absorption parameters and the 10 nm particles had the highest remaining fraction for all absorption parameters. Even though exposure to aluminum nanoparticles may be considered unsafe at very high number concentrations, more studies and experimental data are needed in order to ascertain the actual biological effects on the human condition.

Table 4-1. Composition of Simulated Lung Ultra-Filtrate (SUF)

Compound	Formula Wt.	Milli-moles/L	g/L
NaCl	58.4	116	6.7790
NH ₄ Cl	53.49	10	0.5349
NaHCO ₃	84.01	27	2.2683
NaH ₂ PO ₄ -H ₂ O	137.998	0.2	0.1656
Na ₃ Citrate – H ₂ O	294.19	0.2	0.0558
Glycine	75.07	5.0	0.3754
L-Cysteine	175.63	1.0	0.1756
Hydrochloride			
DTPA	393.35	1.0	0.0787
H ₂ SO ₄ (Conc)	98.08	0.01	0.03 ml/L
CaCl ₂ – ₂ H ₂ O	146.92	0.2	0.294
ABDC	0.005	5.0e-3	0.1 ml/L

DTPA – diethylenetriaminepentaacetic acid

ABDC – alkylbenzyl-dimethyl-ammonium chlorides 50% by volume

Table 4-2. Aluminum volume weighed mean particle size parameters and dissolution rate constants

Material (H-2 Aluminum)	SSA (m ² /g)	MMD (μm)	λ (day ⁻¹)	a (Equation Constant)	\bar{k}_e (g/cm ² - day)	$\frac{D[4,3]_1}{D[4,3]}$	\bar{k}_c (g/cm ² -day)
Experimental	3.3352 ± 0.0344	3.5	0.0051 ± 0.0001	1.0018 ± 0.007	3.5E-7 ± 0.0012	0.85	3.0E-7 ± 0.0012
ICRP Default Value for Medium Rate	Based on Uniform Sphere	Selected by User	0.0050	1	Depends on Surface Area & Solubility (S,M,F)	1.0	NA

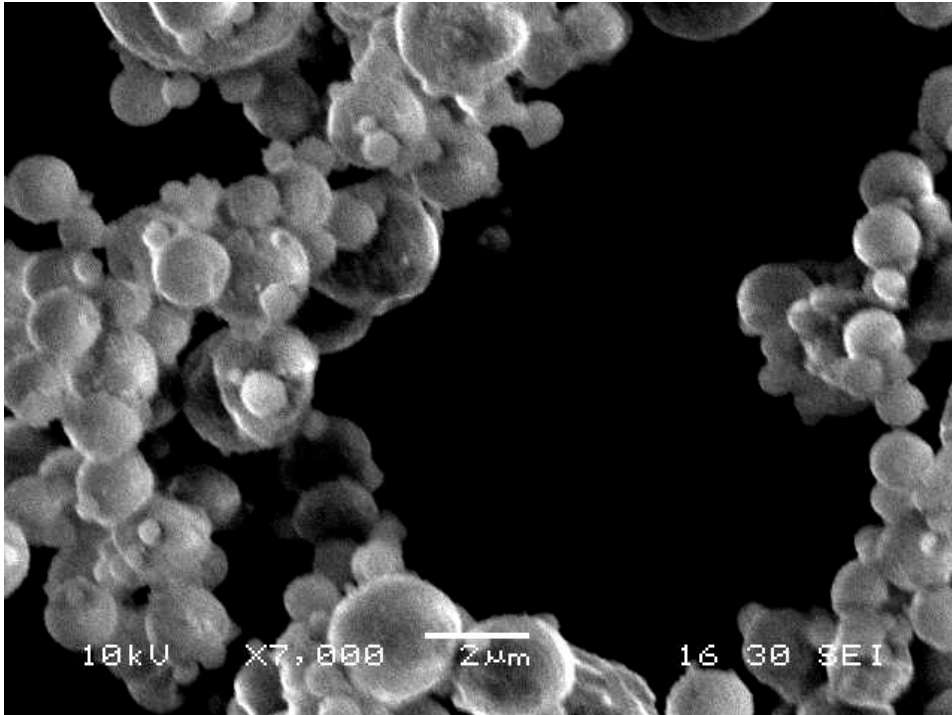


Figure 4-1. Scanning electron micrograph (SEM) of H-2 aluminum powder used in the dissolution tests.



Figure 4-2. Image of a dissolution setup, the mass flow meters control gas flow, equal length tubing for constant pressure drop across all cells with temperature and pH monitoring. A heated bath with water pump ensures a constant temperature in each dissolution cell.

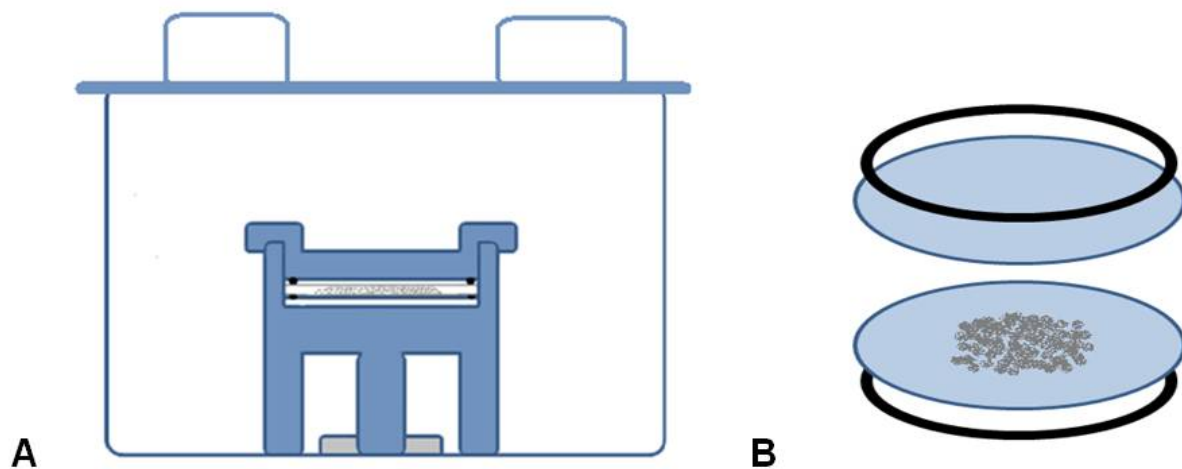
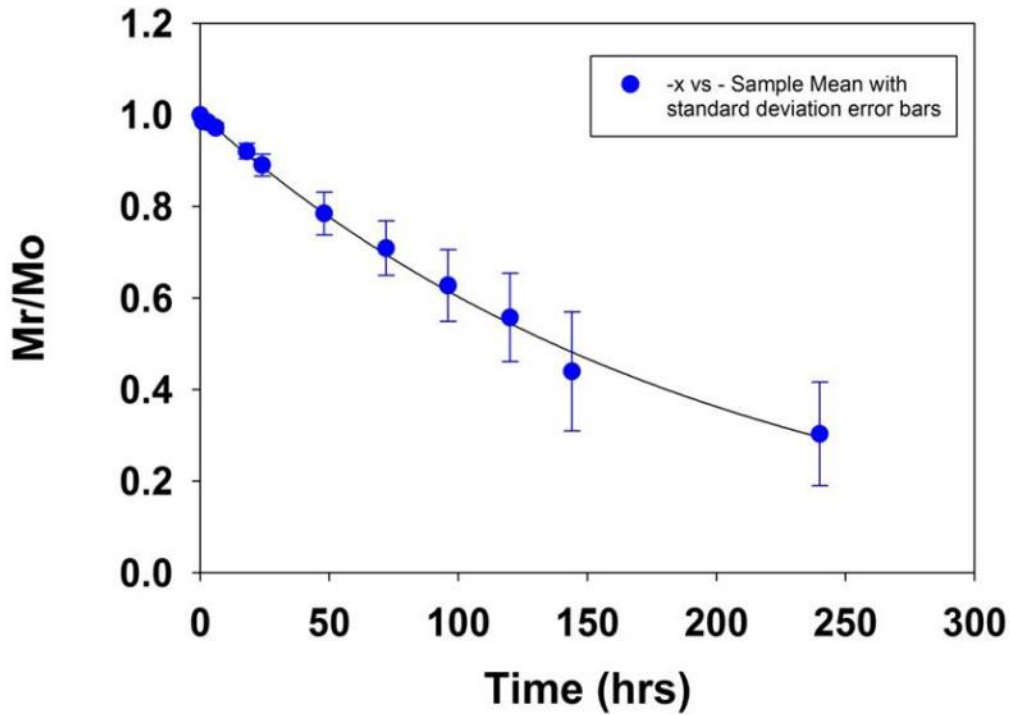


Figure 4-3. A sketch of dissolution cell with stir bar in the center under filter holder. A) dissolution cell with pH and solvent solution sampling ports, and (B) filter sandwich of aluminum powder with 0.10 μm membranes.



B

Point	1	2	3	4	5	6	7	8	9	10	11	12
Time	0	1	3	6	18	24	48	72	96	120	144	240
Residual	0.001	0.017	0.002	0.000	0.006	0.004	0.000	0.015	0.013	0.014	0.040	0.008

Figure 4-4. Dissolution plot for H-2 aluminum in SUF. A) The mean of each sample group is plotted with one standard deviation error bar. The standard deviation in each data set increases with time this is due to the many removals of samples and make-ups (additions of SUF after sample removal) from the dissolution cell and evaporation of solvent even when closed vessels are used. B) List of residuals at each point, these are the differences between the mean sample value and the equation fit at each sampling time point.

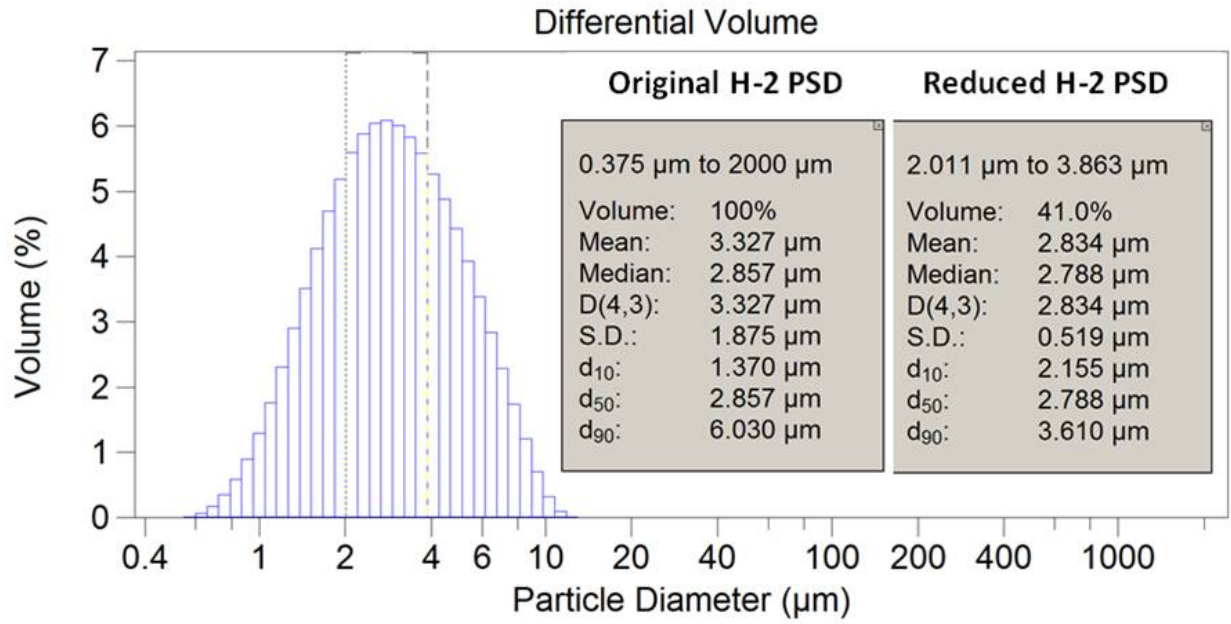


Figure 4-5. PSD for H-2 D[4,3] and the adjusted section for D[4,3]₁ with an arithmetic std of $\sigma \leq 0.5$.

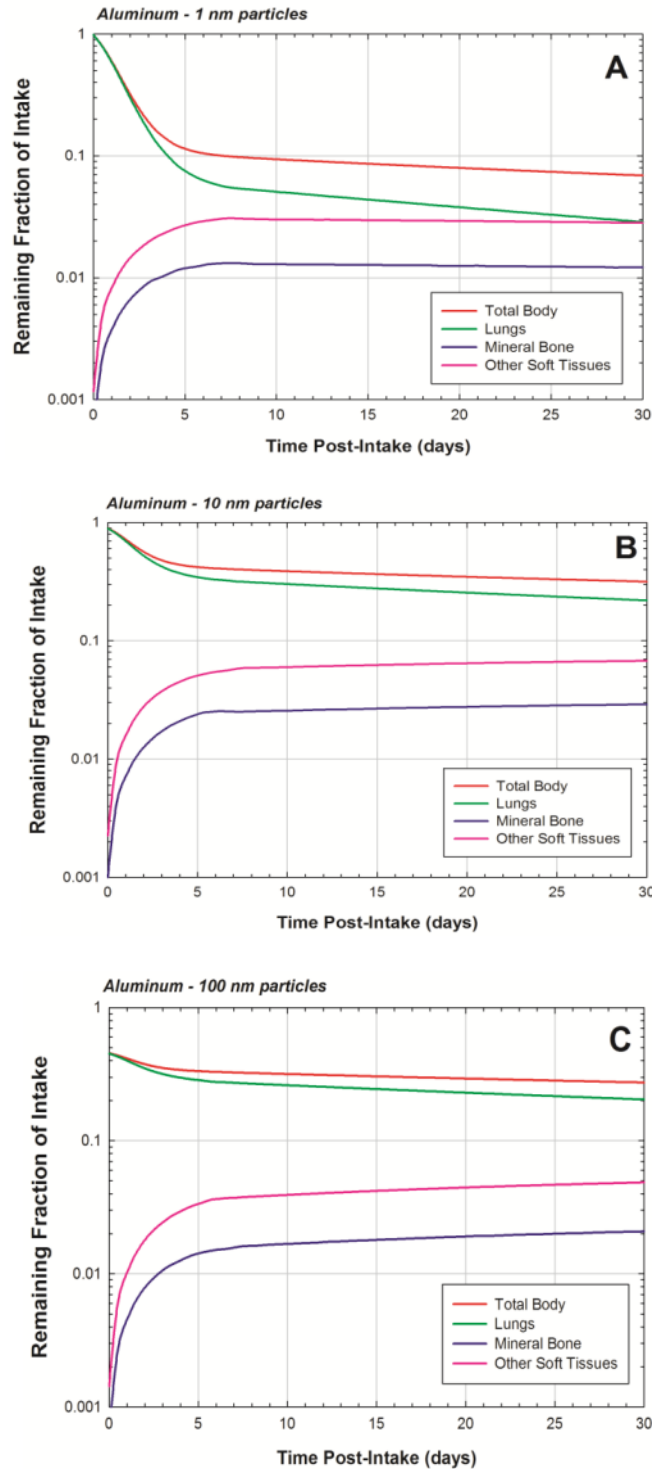


Figure 4-6. A plot of the remaining mass fractions of inhaled aluminum. A) 1 nm, B) 10 nm, and C) 100 nm particle size as a function of time in the total body, lungs, mineral bone, and other soft tissues using the ICRP default values for lung fluid solubility (Bolch 2012).

CHAPTER 5 SUMMARY

The work completed in this dissertation supports several areas of significant research concerning particle dynamics driven by the product gases of a condensed energetic material and the determination of the dissolution rate constant of aluminum from a polydistributed powder sample. The research and the conclusions developed in Chapters 2 and 3 support the need by the energetic materials community to improve its understanding of particle dynamics present in a blast wave at the individual particle level. The determination of the dissolution rate constant in simulated lung ultrafiltrate (SUF) in Chapter 4 supports the need to determine if the current default value identified in the ICRP-66 lung model is accurate for aluminum. Further details are addressed by chapter in the following summary.

Chapter 2 concerns the application of particle image velocimetry (PIV) with the determination of particle velocities generated in explosively driven blast waves at a standoff distance of 1.0 m. The technique was explained in detail and the unique capabilities of imaging small particle positions and determining their velocities within the blast wave was explored. The field of view (FOV) provided a large sample of valid particle images which translated into several thousand vectors for mean velocity determination. This capability along with the particle size distribution provides an understanding of several phenomena including the estimate of the energy partitioning between the light product gases, shock wave, and the solid particle component. The result demonstrated that adjustments to the different components within the explosive can be made to fine tune the desired effect. Additional benefits derived from the technique included identification of the degree of dispersion and agglomeration of

particles within the particle field. This is a significant capability when applied to position locations within the expansion zone with different material types. Finally, the cumulative value of the derived data was shown to be significant with respect to validation of numeric models simulating multiphase flow phenomena such as particle-particle interaction wake effects and mixing turbulence.

In Chapter 3, the further application of the techniques developed in Chapter 2 for imaging particle fields and determining their particle velocities were applied in combination with the standard technique of early time (0-125 μ s) imaging using a high speed framing camera (HSFC). The synergistic effect of combining the two techniques provided the ability to determine particle mean drag coefficients and additional understanding of particle structure development during early time acceleration of particles. These findings also influenced the further development of numeric models and the fine tuning of energetic materials. The reproducibility of test results was demonstrated in the research. This information is significant and relevant for the test design because of the many sources of error to be controlled in the explosive system and experimental process. Some of these sources include the buildup, equipment setup and the inherent error of the measuring technique. The testing process was demonstrated as being in control by providing velocity data which met several statistical tests for normality.

In Chapter 4, the dissolution rate constant for aluminum was determined for H-2, a standard commercial powder frequently used in the research of energetic and reactive formulations. The dissolution rate constant is specific to each material and can be influenced by the materials shape and size distribution. Most researchers process the

material to make it monodistributed (i.e. the same particle diameter) before the rate constant is determined; certain assumptions of the physical properties such as spherical shape and material homogeneity are also assumed. For this portion of the study the particle size distribution (PSD) and its volume moments were determined and adjustments in the final rate constant made to correct the sample from a normal distribution to a monodistribution using a ratio of the volume moments from the two distributions. The technique can be used on powders that are not monodistributed providing more flexibility in the samples that are to be analyzed. The mathematical technique used in this research was adapted from Tinke et al. (2007) numerical research. The second portion of Chapter 4 compared the experimental rate constants to the default values for relatively insoluble materials listed in the ICRP Publication 66 Human Respiratory Tract model. The default values are listed as either fast, medium, or slow (Type F, M, or S, respectively) with each having a different clearance rate $\lambda(t)$. This study determined that the clearance rate to blood determined from the experimentally corrected dissolution rate and the specific surface area (SSA) of the particle matched the ICRP value for medium (M) solubility. This finding could support greater confidence in the results provided by simulation tools like IMBA in monitoring workers who become exposed to nano aluminum.

Conclusion 1: The adaptation of particle image velocimetry for determination of small particle velocities in high luminescent blast waves provides good vector data if particle densities are not excessive and individual particle images do not overlap.

Conclusion 2: The synergistic effect of using a high speed framing camera (HSFC) in conjunction with particle image velocimetry (PIV), provides the capability to

determine the evolution of several particle physics phenomena. These include drag coefficients, particle structure formation, agglomeration, particle velocity gradients and at high image resolution particle collision and burning of reactive particles.

Conclusion 3: The comparison of experimentally determined velocity values with numeric values from computational fluid dynamics (CFD) models can support complex algorithm development and refinement. Validation of CFD hydrocodes with experimentally determined values is necessary to quantify the significance of assumptions made in complex flow regimes.

Conclusion 4: The experimental absorption rate to blood value (λ) for aluminum was found to match the ICRP value for moderate materials. This is significant because it provides confidence that past and future simulations using the ICRP default value for aluminum are correct and it verifies that the logic for assigning aluminum to the moderate group was sound.

Conclusion 5: The ability to determine the dissolution rate constant from normally distributed powders and correct them using volume moments to a standardized value associated with monodistributed powders can allow assessment of industrially supplied powders without complex processing to a monodistributed sample. This allows easier use of dissolution data to support simulation programs like IMBA for material exposure prediction.

Based on the doctoral research presented in the dissertation, future research is recommended on the following topics:

1. It has been demonstrated that PIV is an effective imaging technique for determining particle velocities in blast waves. PIV also provides the ability to image particle phenomena unique to the specific material such as burn or agglomeration. The luminescence produced does become a factor in the

effectiveness of the cross correlation algorithm to identify valid images in a high noise environment. Additional research to reduce background noise and enhance the cross correlation algorithm for this specific purpose would be helpful in improving the identification of image pairs.

2. Because of the short time scales in the detonation and expansion process, high velocities of particle material are produced. Further research into improvements in CCD chip memory and data storage is needed to increase the number of camera images per test and allow for a great understanding of the unfolding expansion event. In the interim, further research into the application of multi-camera imaging is needed to provide information on the evolving particle cloud to include turbulent mixing in three dimensional space. This contribution would significantly aid in the further development of numeric models and their validation of turbulent mixing.
3. Further study of other charge types and geometries (i.e. spherical) are needed to examine the different effects of particle laden explosives and explosive with particle beds surrounding the high explosives.
4. Research providing the gas velocities of different charge configuration would be beneficial since most of these values are computed from numeric models under strict assumptions of the gas properties such as viscosity, temperature and gas component make-up.
5. Further research into the dissolution rates of metals commonly used in energetic materials is needed to provide a full range of confidence in the absorption rate to blood for new computational models where mixtures of metals are used. Computational models which do not have a radioactive component are needed to reduce the error and analysis burden now inherent in IMBA like programs.

APPENDIX CENTER OF MASS PROGRAM FOR PARTICLE FIELDS

```
% MAT.LAB center mass.m
% Developed for Mike Jenkins, programmed by E. Herbold 4/21/09

% Developed for determining the center of mass of the aluminum and tungsten
% particle flow fields shown in the PIV .bmp files.

clear,clc

filenames = dir('*BMP');
nofiles = length(filenames);

disp('The files in this directory are:');
for i = 1:nofiles
    fprintf('  %i: %s \n',i,filenames(i,1).name);
end

fileno = input('Which file would you like to process? \n');
if fileno>nofiles
    error('File # too high');
end

%rect = [24.51 131.51 378.98 33.98];
pic = imread(filenames(fileno,1).name);
figure(1),clf
imagesc(pic);
nFrames = 1;
first_frame = pic;
frame_regions = first_frame;

seg_cyl = false([size(pic,1) size(pic,2) nFrames]);
se_disk = strel('rectangle',[2,2]);

gfr = rgb2gray(pic);
ans = 'n';
val = 0.1;
while ans == 'n'
    bw1 = im2bw(pic,val); % threshold is determined experimentally
    figure(1),clf
    imagesc(bw1);colormap(gray);
    ans = input('does this look ok (y/n)? \n','s');
    if ans == 'n'
        fprintf('threshold value is %5.4g \n',val);
        val = input('what would you like the threshold to be [between 0 and 1]?
\n');
    end
end

bw = imopen(bw1,se_disk);
```

```

bw = imclearborder(bw);

[sizey,sizeX] = size(bw1);

% the overall centroid is computed in the following way.
% It is assumed that each pixel is scaled to have unit length dimensions.
% The expression for the composite centroid of a region is
%
% C_x = (int(X*dA))/A;
% C_y = (int(Y*dA))/A;
%
% In a discrete form, the centroid becomes
%
% C_x = sum(X_i*(dx_i*dy_i))/A_tot
% C_y = sum(...)/...
%
% this is the form of the algorithm below
cnt = 0;
cx = 0;
cy = 0;
for i = 1:sizeX
    for j = 1:sizey
        cnt = cnt + bw1(j,i);
        cx = cx + i*bw1(j,i);
        cy = cy + j*bw1(j,i);
    end
end
cx = cx/cnt;
cy = cy/cnt;

figure1 = figure(1);
imshow(pic)
hold on
plot(0,0,'bo',cx,cy,'ro','MarkerFaceColor','r','Markersize',8)
% Create textbox
annotation(figure1,'textbox',[0.2597 0.01331 0.4563 0.03685],...
    'String',{sprintf('The centroid is %0.5g pixels from the left and %0.5g
pixels from the top',cx,cy)},...
    'FontSize',14,...
    'FontName','Times New Roman',...
    'FitBoxToText','off');
hold off

fprintf('\n The centroid is %0.5g pixels from the left and \n %0.5g pixels
from the top \n',cx,cy);

%pname = strcat(filenamees(fileno,1).name,'_cent.eps');
%print(figure1, '-dpSC', pname);
%system(strcat('open -a Texshop, ',pname));

```

LIST OF REFERENCES

- Adrian, R.J., 1991. Particle imaging techniques for experimental fluid mechanics. *A. Rev. Fluid Mech.* 23, 261–268.
- Anderson, J.D., 1997. *Fundamentals of Aerodynamics*. (4th ed.). McGraw-Hill. ISBN 0071254080.
- Ansoborlo, E., Henge-Napoli, H., Chazel, V., Gilbert, R., and Guilmette, R.A., 1999. Review and critical analysis of available *in vitro* dissolution tests. *Health Phys.* 77(6), 638-645.
- Asbach, C., Fissan, H., Stahlmecke, B., Kuhlbusch, T.A.J., Pui, D.Y.H., 2009. Conceptual limitations and extensions of lung-deposited nanoparticle surface area monitor (NSAM). *J. Nanopart. Res.* 11, 101-109.
- Asgharian, B., Price, O.T., 2007. Deposition of ultrafine (nano) particles in the human lung. *Toxicol.* 19(13), 1045-1054.
- Balakrishnan, K., Genin, F., Nance, D.V., Menon, S., 2009. Numerical study of blast characterization from detonation of homogeneous explosives. *Shock Waves* 20, 147-162.
- Balakumar, B.J., Adrian, R.J., 2004. Particle image velocimetry in the exhaust of small solid rocket motors. *Exp. Fluids* 36, 166–175.
- Birchall, J.A., 2003. *Users manual for IMBA professional series*, Richland, WA: ACJ & Associates, Inc.
- Bolch, W., 2012. Personal communication: plots of the remaining mass fractions of inhaled aluminum. University of Florida Fig. 4-6, p. 105.
- Braydich-Stolle, L., Hussain, S., Schlager, J., Hofmann, C., 2005. In vitro cytotoxicity of nanoparticles in mammalian germline stem cells, *Toxicol. Sci.* 88(2), 412-419.
- Brunauer, S., Emmett, P.H., Teller, E., 1938. Adsorption of gas in multimolecular layers. *J. of ACS* 60, 309-319.
- Buxton, D.B., Lee, S.C., Wickline, S.A., Ferrari, M. and Blood Institute Nanotechnology Working Group, 2003. *Circulation* 108(22), 2737-2742.
- Chapman, D.L., 1899. On the rate of explosion in gases. *Philosophical Magazine* 47, 90-104.
- Cheng, M.-D. and Jenkins C.M., 2005. Production and dynamics of ultrafine and fine particles in contained detonations of aluminium energetics. *J. Aerosol Sci.* 36(1), 1-12.

- Chinook keyword input manual, Software manual #SM-07-06, Rev.27, Martec Limited, 1888 Brunswick Street, Ste 400, Halifax, Nova Scotia B3J3J8, Canada, 26 Apr., 2006.
- Cooper, P.W., 1997. Explosive engineering. Wiley & Sons, New York, NY.
- Donahue, L., Ripley, R.C., Horie, Y., Jenkins, C.M., & Zhang, F., 2007. Cylindrical explosive dispersal of metal particles. APS15.
- Donaldson, K., Borm, P.J.A., Oberdörster, G., Pinkerton, K.E., Stone, V., Tran, C.L., 2008. Concordance between in vitro and in vivo dosimetry in the proinflammatory effects of low-toxicity, low-solubility particles: the key role of the proximal alveolar region. *Inhalation Tox.* 20, 53-62.
- Donaldson, K., Mills, N., MacNee, W., Robinson, S., Newby, D., 2005. Role of inflammation in cardiopulmonary health effects of PM, *Tox. Applied Pharm.* 207, 483-488.
- Döring, W., 1943. "Über Detonationsvorgang in Gasen [On detonation processes in gases]", *Ann. Phys.* 43, 421-436, ISSN 0003-4916.
- Eidson, A. F., 1990. In vitro dissolution of silicon carbide whiskers in SUF, Lovelace Inhalation Toxicology Research Institute, SOP #0898.
- Engelhardt, C.M. Numerical modeling of heterogeneous high explosives, AIAA - 40th thermophysics conference, 6(2008).
- Ferrari, M., 2005. Cancer nanotechnology: opportunities and challenges. *Nat Rev Cancer* 5,161-171.
- Frost, D.L., Goroshin, S., Levine, J., Ripley, R., Zhang, F., 2005. Critical conditions for ignition of aluminum particles in cylindrical explosive charges, 14th APS Conference on Shock Compression of Condensed Matter, Baltimore, Maryland.
- Frost, D.L., Ornthanalai, C., Zarei, Z., Tanguay, V., and Zhang, F., 2007. Particle momentum effects from the detonation of heterogeneous explosives. *J. of Applied Phys.* 101, 113-129.
- Frost, D.L., Tanguay, V., Zhang, F., 2007. Particle momentum from the detonation of heterogeneous explosives. *J. Appl. Phys.* 101, 113-129.
- Frost, D.L., Zhang, F. and McCahan, S., 2002. Critical conditions for ignition of metal particles in a condensed explosive. 12th. Int. Detonation Symposium. San Diego, Ca.

- Frost, D.L., Zhang, F., 2006. The nature of heterogeneous blast explosives. In: Proceedings of the 19th International Symposium on Military Aspects of Blast and Shock. Calgary, AB, Canada.
- Fuchs, N.A., 1964. The mechanics of aerosols. Macmillan Co., New York. N.Y.
- Gagliardi, F.J., Chambers, T.D., Tran, Tri-D. Small-scale performance testing for studying new explosives. 6th VACETS Technical International Conference, UCRL-CONF-212196, Milpitas, Ca, USA, June 4, 2005.
- Hinds, W.C., 1999. Aerosol Technology: Properties, Behavior, and Measurement of Airborne Particles. second ed. New York, John Wiley & Sons, Inc.
- International Commission on Radiological Protection, 1994. Human respiratory track model for radiological protection. ICRP Publication 66, Elsevier Science, Tarrytown NY.
- Jouguet, J. C.E. (1905), "Sur la propagation des reactions chimiques dans les gaz" [On the propagation of chemical reaction in gases], *Journal des Mathématiques Pures et Appliquées* Series 6, 1, 347-425.
- Keshavarz, M.H., 2006. Detonation temperature of high explosives from structural parameters. *J. Haz. Materials* A137.
- Lewinski, N., Colvin, V. and Drezek, R., 2008. Cytotoxicity of nanoparticles. *Small*, 4:26-49. doi: 10.1002/smll.200700595
- Liang, J., 2006. Chinese siege warfare: Mechanical artillery & siege weapons of antiquity. ISBN 981-05-5380-3.
- Ling, Y., Haselbacker, A., Balachandar, S., 2009. Transient phenomena in one-dimensional compressible gas-particle flows. *Shock Waves* 19, 67-81.
- Marra, J., Voetz, M., Kiesling, H-J., 2010. Monitor for detecting and assessing exposure to airborne nanoparticles. *J. Nanopart. Res.* 12, 21-37.
- Mercer, T.T. (1969), On the role of particle size in the dissolution of lung burdens. *Health Physics* 13, 1211-1221.
- Milne, A.M. (2000). Detonations in heterogeneous mixtures of liquids and particles. *Shock Waves* 10, 351.
- Murphy, M.J., Adrian, R.J., Stewart, S.D., Elliott, G.S., Thomas, K.A., Kennedy, J.E., (2005). Visualization of blast waves created by exploding bridge wires. *J. Visual.* 8, 125-135.

- Oberdörster, G., Oberdörster, E., Oberdörster, J., 2005. Nanotoxicology: An emerging discipline involving from studies of ultrafine particles. *Env. Health Perspectives* 113, 823-836.
- Oberdörster, G., Sharp, Z., Atudorei, V., Elder, A., Gelein, G., Kreyling, W., Cox, C., 2004. Translocation of inhaled ultrafine particles to the brain. *Inhal Toxicol.* 16(6-7), 437-445.
- Oesterling, E., Chopra, N., Gavalas, V., Arzuaga, X., Lim, E.J, Sultana, R., Butterfield, D.A., Bachas, L., Hennig, B., 2008. Alumina nanoparticles induce expression of endothelia cell adhesion molecules. *Toxicology Letters* 178, 160-166.
- Palazuelos, M., Erdos, G.W., Moraga, D.A., Moudgil, B.M. Powers, K.W., 2006. Impact of nano to micron size particle characteristics on in vitro aluminum particle toxicology. *The Toxicologist* 319.
- Peters, A., Dockery, D.W., Muller, J.E., Mittleman, M.A., 1997. Increased plasma viscosity during air pollution episode: a link to mortality?, *Lancet* 349, 1582-1587.
- Petrovich, M.V., 2007. MVPstats: MVP Programs, ver. 20071215.
- Richards, D.W., De Angelis, R.J., Kramer, M.P., House, J.W., Cunard, D.A., Shea, D.P., 2004. Shock-induced deformation of tungsten powder. *International Centre for Diffraction Data, Advances in X-ray Analysis* 47, 351-356.
- Ripley, R.C., Zhang, F., Lien, F. Detonation iteration with metal particles in explosives. *13th Symposium (International) on Detonation*, Norfolk, VA., 2006.
- Ripley, R.C., Zhang, F., Lien, F., Fue-Sang. Acceleration and heating of metal particles in condensed explosive detonation, CP955, *APS Conference on Shock Compression of Condensed Matter*, Baltimore, MD, edited by M. Furnish, M. Elert, T. Russell, and C. White, American Institute of Physics, Melville, NY, 2007.
- Saito, T., Marumoto, K. and Takayama, K., 2003. Numerical investigations of shock waves in gas-particle mixtures. *Shock Waves* 13, 299-322.
- Schmitt, R.G., Thompson, A.P., Aidun, J.B., 2010. Enabling R&D for accurate simulation of non-ideal explosives. Sandia Report, SAND2010-6831, Sandia National Laboratory, Albuquerque, New Mexico.
- Sdraulig, S., Franich, R., Tinker, R.A., Solomon, S., O`Brian, R., Johnston, P.N., 2008. In vitro dissolution studies of uranium bearing material in simulated lung fluid. *J. Enviro. Radio.* 99(3), 527-538.
- Seaton, A., MacNee, W., Donaldson, K., Godden, D., 1995. Particulate air pollution and acute health effects, *Lancet* 345, 176-178.

- Stefaniak, A.B., Day, G.A., Hoover, M.D, Breysse, P.N., Scripsick, R.C., 2006. Differences in dissolution behavior in a simulant fluid for single-constituent and multi-constituent materials associated with beryllium sensitization and chronic beryllium disease. *Tox. in Vitro* 20, 82-95.
- Stitou, A. & Riethmuller, M.L., 2002. Progress in PIV-PTV methods: application to concentration measurements, 11th International Symposium on Application of Laser Techniques to Fluid Mechanics, Lisbon, Portugal, July 8-11, VKI RP 2002-36.
- Tanguay, V., Higgins, A.J., Zhang, F., 2007. A simple analytical model for reactive particle ignition in explosives. *Prop. , Explosives, Pyrotechnics* 32, 371-384.
- Tinke, A.P., Vanhoutte, K., De Maesschalck, R., Verheyen, S., De Winter, H., 2005. A new approach in the prediction of the dissolution behavior of suspended particles by means of their particle size distribution. *J. Pharm. Biomed. Anal.* 39, 900-907.
- Von Neumann, J. (1963), "Theory of detonation waves. Progress report to the National Defense Research Committee Div. B., OSRD-549", in Taub, A.H., *John von Neumann: Collected Works, 1903-1957*, 6, New York: Pergamon Press, ISBN 97880080095660.
- Wagner, A.J., Bleckmann, C.A., Murdock, R.C., Schrand, A.M., Schlager, J.J., Hussain, S., 2007. Cellular interaction of different forms of aluminum nanoparticles in rat alveolar macrophages, *J. Phys. Chem. B* 111, 7353-7359.
- Zarei, Z., Frost, D.L., Timofeev, E.V., 2011. Numerical Modeling of the entrainment of particles in viscous supersonic flow. *Shock Waves* 21, 341-355.
- Zel'dovich, Ya.B., 1940. "К теории распространения детонации в газообразных системах [On the theory of the propagation of detonations on gaseous system]", *Zh. Eksp. Teor. Fiz.* 10, 542-568.
- Zhang, F., Frost, D.L., Thibault, P.A., Murray, S.B., 2001. Explosive dispersal of solid particles. *Shock Waves* 10, 431-443.
- Zhang, F., Thibault, P.A. and Link, R., 2003. Shock interaction with solid particles in condensed matter and related momentum transfer. *Proc. R. Soc. Lond. A.* 459, 705-726.
- Zhang, F., Yoshinaka, A., Frost, D., Ripley R.C., Kim, K., Wilson W., 2006. Casing Influence on ignition and reaction of aluminum particles in an explosive, 13th International Detonation Symposium, Norfolk, USA.

BIOGRAPHICAL SKETCH

Charles M. Jenkins was born in Florence, Alabama and move to Phoenix, Arizona with his family where he graduated from Central High School in 1974. Later, he graduated from Phoenix College with an associate's degree while working for Reynolds Metals Company. He then pursued a Bachelor of Science degree in chemical engineering and graduated from the University of South Alabama in 1983. While working as an engineer at Eglin AFB, Florida, he began a Master of Aeronautical and Aerospace Science degree from Embry-Riddle Aeronautical University, from which he graduated in 1993. After having worked for one additional year as a project engineer, he then began a Master of Environmental Engineering from the University of South Florida which he completed in 1998. Changing professional directions in 2004, from production and test program management he began working in the field of energetic materials research at the Air Force Research Laboratory, Energetic Materials Branch for High Explosive Research and Development (HERD) facility at Eglin AFB, Florida. During this period he began a degree program this time for a Doctor of Philosophy in environmental engineering concentrating in aerosol science under Dr. Chang-Yu Wu in the Environmental Engineering and Science Department at the University of Florida. Additional course work in particle toxicology was accomplished through the Center for Environmental and Human Toxicology at the University of Florida lead by Dr. Stephen Roberts. Currently, Charles is investigating the kinetics of reactive materials under high temperature and shock induced pressures.